Bacillus subtilis YisK possesses oxaloacetate decarboxylase activity and exhibits Mbl-dependent localization

Tingfeng Guo,[1] Anthony M. Sperber,[1] Inna V. Krieger,[1] Yi Duan,[1] Veronica R. Chemelewski,[1] James C. Sacchettini,[1,2] Jennifer K. Herman[1]

AUTHOR AFFILIATIONS See affiliation list on p. 18.

ABSTRACT YisK is an uncharacterized protein in *Bacillus subtilis* previously shown to interact genetically with the elongasome protein Mbl. YisK overexpression leads to cell widening and lysis, phenotypes that are dependent on *mbl* and suppressed by *mbl* mutations. In the present work, we characterize YisK's localization, structure, and enzymatic activity. We show that YisK localizes as puncta that depend on Mbl. YisK belongs to the fumarylacetoacetate hydrolase (FAH) superfamily, and crystal structures revealed close structural similarity to two oxaloacetate (OAA) decarboxylases: human mitochondrial FAHD1 and *Corynebacterium glutamicum* Cg1458. We demonstrate that YisK can also catalyze the decarboxylation of OAA (K_m = 134 µM, K_{cat} = 31 min^{-1}). A catalytic dead variant (YisK E148A, E150A) retains wild-type localization and still widens cells following overexpression, indicating these activities are not dependent on YisK catalysis. Conversely, a non-localizing variant (YisK E30A) retains wild-type enzymatic activity *in vitro* but localizes diffusely and no longer widens cells following overexpression. Together, these results suggest that YisK may be subject to spatial regulation that depends on the cell envelope synthesis machinery.

IMPORTANCE The elongasome is a multiprotein complex that guides lengthwise growth in some bacteria. We previously showed that in *Bacillus subtilis*, the overexpression of an uncharacterized putative enzyme (YisK), a perturbed function of the actin-like elongasome protein Mbl. Here, we show that YisK exhibits Mbl-dependent localization. Through biochemical and structural characterization, we demonstrate that, like its mitochondrial homolog FAHD1, YisK can catalyze the decarboxylation of the oxaloacetate to pyruvate and CO_2. YisK is the first example of an enzyme implicated in central carbon metabolism with subcellular localization that depends on Mbl.

T he bacterial cell envelope serves essential functions in nutrient uptake, secretion, energy production, morphogenesis, and reproduction and acts as a physical barrier against immune detection, antimicrobials, toxic metabolites, and bacteriophages. In addition, the envelope's peptidoglycan (PG) layer helps protect the integrity of the cytoplasmic membrane. A highly tensile polymer, PG is elastic enough to allow for expansion and contraction during osmotic shifts but strong enough to withstand multiple atmospheres of pressure (1–4). The envelope layers external to PG vary in composition by genus, species, and growth condition. In the Gram-positive bacterium *Bacillus subtilis*, the outer layers are composed of the anionic polymers teichoic and teichuronic acid, extracellular proteins, exopolysaccharides, and poly-γ-glutamic acid (5–7).

In many rod-shaped bacteria, including *B. subtilis*, the lengthwise incorporation of new PG during growth is governed by the elongasome, a membrane-associated multiprotein complex that guides growth along the cell's long axis (8). The elongasome is thought to be scaffolded by the actin-like protein MreB (9). MreB dynamically polymerizes and, along with its associated factors MreC and MreD (10), helps recruit enzymes that insert, modify, and hydrolyze PG (8, 11). Some bacteria possess multiple MreB paralogs, and *B. subtilis* encodes three: MreB (encoded in the conserved *mreBCD* operon), Mbl, and MreBH. Each *B. subtilis* paralog can support the maintenance of rod shape and viability if expressed at sufficient levels, consistent with functional redundancy (12). At the same time, the paralogs also possess some specialized activities (13–16). MreBH facilitates the function of LytE, a PG endopeptidase associated with envelope stress (14, 16, 17), whereas Mbl influences the activity of CwlO, a major PG endopeptidase utilized during cell growth (16). CwlO activity is also dependent on the conserved ABC transporter FtsEX (16, 17) and perturbed in the absence of two recently discovered cofactors, SweC and SweD (18).

In a prior study, we found evidence of a genetic interaction between Mbl and a putative enzyme, YisK (BSU10750) (19). YisK overexpression causes cell widening and lysis, which can be suppressed by specific substitutions in Mbl or deleting *mbl* in a background that relieves Mbl essentiality (Δ*ponA*, encoding PBP1A) (19). These results indicate YisK and Mbl interact at least genetically and are consistent with *yisK* overexpression disrupting Mbl function.
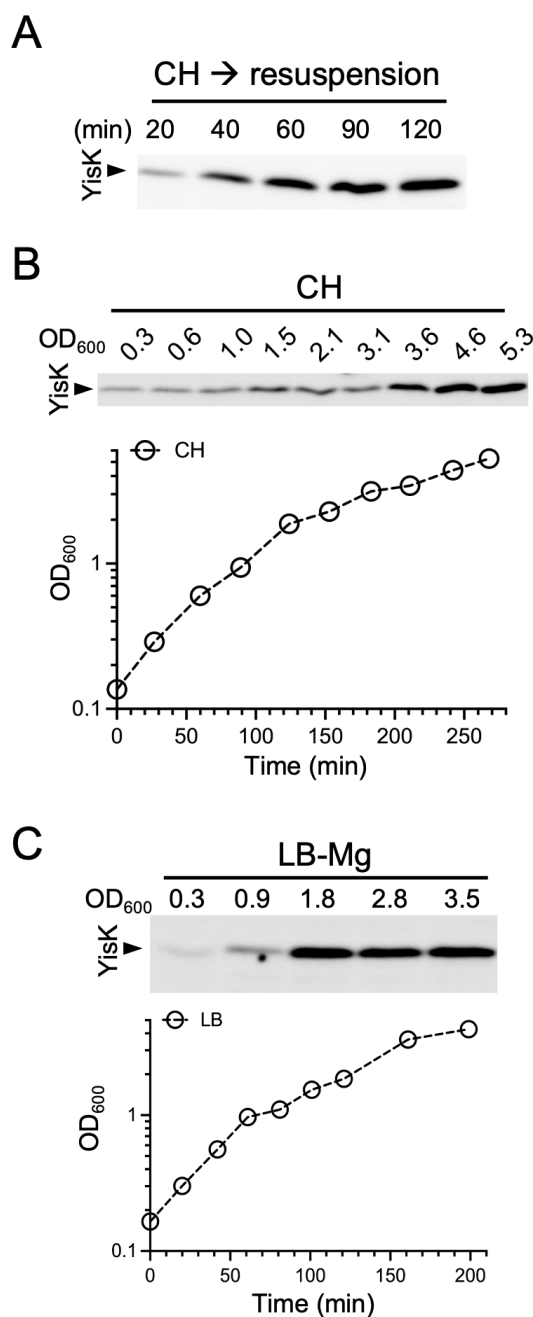
YisK is in the SigH regulon (20), induced during the early stages of sporulation (19), and classified as a general starvation protein (21). Based on transcriptomic and proteomic analysis, YisK is also expressed in a variety of other conditions including exponential growth in M9 minimal medium (22–24). In M9 containing glucose and malate as carbon sources, YisK is estimated to be present at ~1,000 copies per cell across exponential, transition, and stationary phases of growth (23). Thus, despite being in the SigH regulon, YisK is clearly expressed in growth contexts outside of the stationary phase, sporulation, and general starvation.

Based on sequence conservation, YisK belongs to the fumarylacetoacetate hydrolase (FAH) superfamily, a class of catabolic enzymes that catalyze diverse reactions, including dehydrations, decarboxylations, and isomerizations (25). FAH proteins are found in all domains of life and share a common mixed β-sandwich-like fold (26). The catalytic pocket coordinates a divalent metal ion, usually Mg^{2+}, Mn^{2+}, or Ca^{2+}, that is essential for enzymatic activity (27, 28). No FAH proteins are known to be involved in PG synthesis, so possible reasons for the epistatic interaction between YisK and Mbl could not be inferred in the prior study. In the present study, we show that YisK exhibits Mbl-dependent localization, characterize YisK structurally, and demonstrate that YisK can catalyze the decarboxylation of oxaloacetate (OAA) to pyruvate and CO_2.

RESULTS

YisK protein is expressed in CH, LB, and sporulation by resuspension medium

yisK is transcriptionally upregulated in sporulation by resuspension medium or during growth in a rich medium permissive for sporulation, casein hydrosylate (CH) (19). To assess the accumulation of YisK protein under these growth conditions, we performed western blot analysis using polyclonal antibody raised against YisK (Fig. S1). When cells were grown in sporulation by resuspension medium, YisK reached maximal levels around 60 min post-resuspension (Fig. 1A) (19); these data correlate well with the appearance of a green fluorescent protein (GFP) signal from a P_{yisK}-GFP reporter in the same growth conditions (19). In the amino acid-based medium CH, YisK was detectable during exponential growth (OD_{600} 0.3 and 0.6) and reached maximal levels between OD_{600} readings of 3.6 and 4.6 (Fig. 1B). The higher OD_{600} range corresponds to when some cells in the population start to enter the sporulation program in CH (19). We also examined YisK levels in LB supplemented with 10.0 mM $MgCl_2$ (LB-Mg), which permits growth to higher cell densities (29). In LB-Mg, YisK was detectable during early exponential growth

A

CH → resuspension

(min) 20 40 60 90 120

YisK ▶

B

CH

OD_{600} 0.3 0.6 1.0 1.5 2.1 3.1 3.6 4.6 5.3

YisK ▶

Growth curve: OD_{600} vs Time (min), labeled CH

C

LB-Mg

OD_{600} 0.3 0.9 1.8 2.8 3.5

YisK ▶

Growth curve: OD_{600} vs Time (min), labeled LB

FIG 1 Analysis of YisK protein levels during growth. (A) Representative western blot of samples collected during growth in sporulation by resuspension medium. Representative western blots and growth curves from cells grown at 37°C in (B) CH and (C) LB-Mg.

but increased to higher levels at the transition state and beyond (Fig. 1C). From these data, we conclude that YisK accumulates both under conditions favorable for sporulation and in LB-Mg, which does not support sporulation.

YisK forms Mbl-dependent puncta in the cell

Our data suggest that YisK interacts with Mbl based on genetic data (19). Mbl lacks transmembrane domains but localizes as discrete puncta that move circumferentially around the long axis of the cell (30, 31) and give the appearance of helical cables with epifluorescence microscopy (30–32). To determine if YisK also localizes within the cell,

we generated a fluorescent GFP "sandwich" fusion (YisK$_{SW}$-GFP) by introducing GFP into a non-conserved loop in YisK between residues E111 and A112. Cells overexpressing YisK$_{SW}$-GFP from an isopropyl-β-D-thiogalactopyranoside (IPTG)-inducible promoter (P$_{hy}$) were inhibited for growth on LB plates (Fig. 2A) and became wide in LB (Fig. 2B), consistent with the previously reported YisK overexpression phenotypes (19). These results indicate that YisK$_{SW}$-GFP retains the YisK-associated phenotypes.

Next, we used the allelic exchange to replace wild-type *yisK* with *yisK$_{SW}$-GFP* at the native locus. In this strain, *yisK$_{SW}$-GFP* is under the control of the native *yisK* promoter (P$_{yisK}$), and no other copy of *yisK* is present in the cell. Having already established that untagged YisK is expressed when cells are resuspended in a sporulation medium (Fig. 1A) (19), we first monitored YisK$_{SW}$-GFP expression and stability at several timepoints after resuspension using western blot analysis (Fig. 2C). Similar to untagged YisK, YisK$_{SW}$-GFP protein was observable at 40 min and increased in abundance between 40 and 90 min (Fig. 2C). The reduced signal from YisK$_{SW}$-GFP in comparison to the untagged YisK may be due to occlusion of anti-YisK epitopes by the internal GFP tag and/or differences in efficiency of transfer of the different proteins to the membrane. YisK$_{SW}$-GFP was detected as a single band using both anti-YisK and anti-GFP antibodies (Fig. 2C; Fig. S2B), indicating the fusion is not proteolyzed.
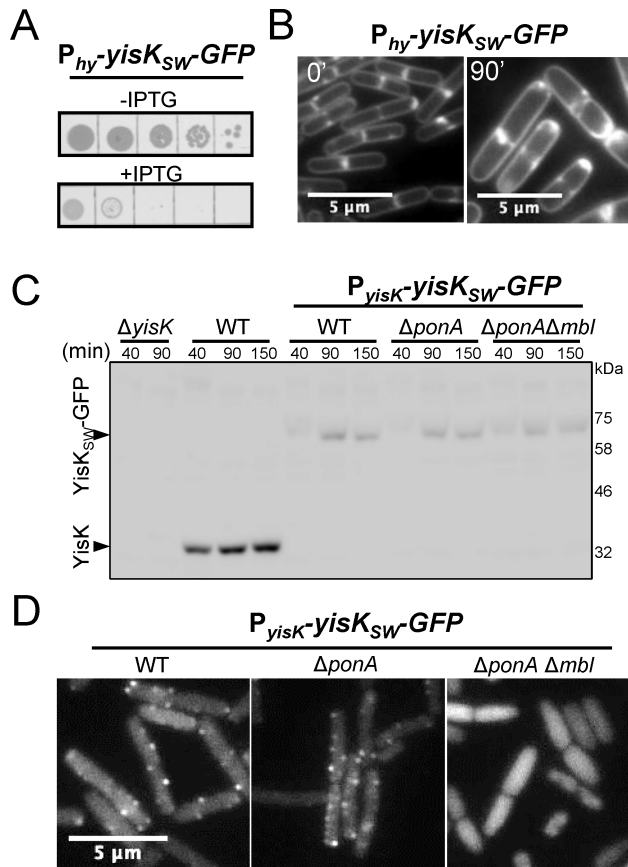
FIG 2 Assays assessing the functionality, expression, and localization of YisK$_{SW}$-GFP. (A) Cells harboring P$_{hy}$-*yisK$_{SW}$-GFP* were spotted on LB without or with 1.0-mM IPTG and incubated at 37°C overnight before imaging. (B) Representative micrograph of cells harboring P$_{hy}$-*yisK$_{SW}$-GFP* following 90-min induction with 1.0-mM IPTG. Membranes were stained with TMA. Images are of the same magnification. (C) Western blot analysis of YisK and YisK$_{SW}$-GFP expression during growth in sporulation by resuspension medium using α-YisK serum. (D) Representative micrographs of cells harboring P$_{yisK}$-*yisK$_{SW}$-GFP* following 40-min growth in sporulation by resuspension medium. Images are of the same magnification and scaled identically in the GFP channel.

Having established that the YisK$_{SW}$-GFP retains YisK-associated phenotypes and is expressed as a stable fusion from the native locus in the resuspension medium, we next monitored YisK$_{SW}$-GFP localization using epifluorescence microscopy. Following growth in the resuspension medium, YisK$_{SW}$-GFP localized both diffusely and in punctate arrangements (Fig. 2D; Fig. S2A). Similar localization was also observed in CH and LB (Fig. S2C and E).

Based on the fact that YisK overexpression perturbs Mbl function and that Mbl is required for YisK to widen cells (19), we hypothesized that YisK might depend on Mbl for localization. To create a strain background permissive for the deletion of *mbl* (11), we deleted *ponA* in the P$_{yisK}$–*yisK-GFP* harboring strain before introducing the *mbl* deletion. In the course of making this strain, we noted that deletion *ponA* resulted in slightly smaller colonies than the wild type and that the deletion strain we obtained from the *Bacillus* Genetic Stock Center contained a growth rate suppressor mutation in *walH* (see strain construction in Fig. S5). Next, we compared YisK$_{SW}$-GFP localization in the Δ*ponA* and Δ*ponA* Δ*mbl* backgrounds to the wild type. As can be seen in Fig. 2D, YisK$_{SW}$-GFP still displayed punctate localization in the Δ*ponA* cells. In contrast, YisK$_{SW}$-GFP was completely diffuse in the Δ*ponA* Δ*mbl* background (Fig. 2D). YisK$_{SW}$-GFP was expressed equivalently and migrated at the same apparent molecular weight in all three backgrounds, indicating that the diffuse signal is not due to clipping/release of GFP or a change in expression levels at the population level (Fig. 2C). From these data, we conclude that YisK exhibits diffuse and punctate localization and that the punctate localization depends on Mbl.

Identification of molecules that stabilize YisK

To gain further insight into YisK function, we sought to characterize YisK biochemically. Following overexpression and purification of a His-tagged fusion of YisK (Fig. 3A), we noted that concentrated YisK solution (~100.0 µM) was tinted slightly pink (Fig. 3B). Since characterized FAH proteins typically coordinate a divalent cation in a conserved active site (25), Mn^{2+} solutions are pink, and the pink color was absent when two of YisK's three metal-coordinating residues were substituted with alanine (YisK E148A, E150A) (Fig. 3B); we hypothesized that YisK most likely coordinated Mn^{2+}. To test, we monitored the thermostability of YisK without and with buffer containing either MnCl$_2$ or MgCl$_2$. Notably, YisK's melting temperature increased by 8°C in the presence of 5.0-mM MnCl$_2$ but differed insignificantly with 5.0-mM MgCl$_2$ (Fig. 3C). Even though purified YisK was pink compared to the E148A E150A variant, the fact that the additional metal was stabilizing suggests that the majority of purified protein lacked a metal cofactor. To estimate the apparent binding affinity (K_a) of YisK for Mn^{2+} and Mg^{2+}, we monitored YisK's thermostability across a gradient of metal concentrations (Fig. 3D and E). From the curves, the apparent K_a of YisK was estimated to be approximately 30 µM for Mn^{2+} and 60 mM for Mg^{2+}. Of note, the intracellular levels of labile Mn^{2+} and Mg^{2+} are estimated to be in the low micromolar and millimolar range, respectively (29, 33, 34). Collectively, these data suggest that YisK likely utilizes Mn^{2+} over Mg^{2+} as a cofactor.

The first YisK crystals (more below) were obtained in the presence of Tacsimate, a mixture of organic acids including L-tartrate. As a positive electron density consistent with tartrate was observed coordinating metal in the active site, we hypothesized that YisK's substrate might possess properties similar to the molecules constituting Tacsimate. Using DSF, we found tartrate markedly increased YisK's thermostability (Table S1). By screening a panel of structurally related compounds, we identified additional molecules that increased YisK's melting temperature as well as those that did not (Fig. S4; Table S1). Oxalomalate, D,L-4-hydroxy-2-ketoglutarate (HOGA), and oxalate all dramatically stabilized YisK, increasing the melting temperature (T_m) by more than 15°C (Fig. S4; Table S1). Glyoxylate, OAA, and pyruvate were not stabilizing in isolation, but the combinations of glyoxylate and either OAA or pyruvate increased YisK's melting temperature significantly (Fig. S4; Table 1). Overall, molecules that stabilized YisK had properties similar to the molecule shown in Fig. 3F.
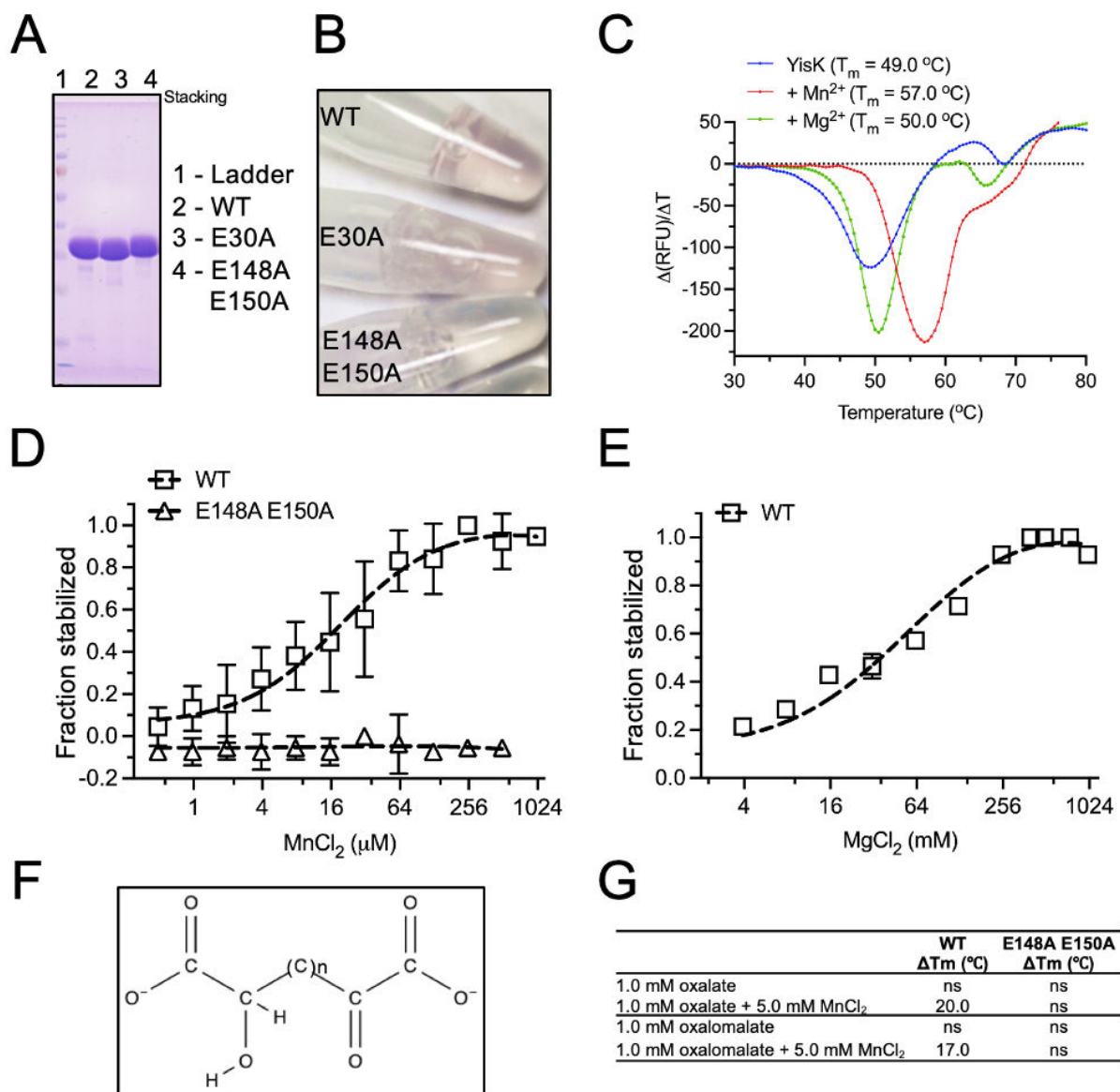
FIG 3 Affinity of YisK for Mn^{2+} as a cofactor. (A) Colloidal Coomassie blue staining of gel of purified proteins used in assays. (B) Purified YisK and YisK variants concentrated to ~100 μM. (C) Differential scanning fluorimetry (DSF) with 10.0-μM YisK (WT) and buffer containing either 5.0-mM $MnCl_2$ or 5.0-mM $MgCl_2$. (D and E) DSF assay with gradient of (D) $MnCl_2$ or (E) $MgCl_2$. The fraction of YisK stabilized was calculated according to the formula: $\Delta T_m/(T_{mMax}-T_{m0})$. (F) Structural elements conserved by compounds that increase YisK's melting temperature in DSF assays. n = 0–2 carbons. (G) DSF assay containing 10.0 μM of the indicated YisK protein. A thermal shift of ≤2.0°C was not considered significant (ns).

Based on the characterized FAH family proteins, YisK's ligand/substrate would bind in the active site by coordinating the Mn^{2+} cofactor. To test if Mn^{2+} was required for compounds to stabilize YisK, we repeated the DSF experiments for oxalate and oxalomalate in buffer without and with the addition of metal; for both compounds, Mn^{2+} was required for stabilization (Fig. 3G). Moreover, the YisK E148A E150A variant (which cannot coordinate Mn^{2+}) was not stabilized by oxalate or oxalomalate even when Mn^{2+} was included in the buffer (Fig. 3G). These results are consistent with the ligands coordinating the metal cofactor in the active site as observed in published FAH crystal structures (25, 28).

TABLE 1 Data collection, phasing and refinement statistics for the YisK structures[a]

	Apo form (8SUU)	Oxalate-bound (8SKY)	4-Hydroxy-2-oxoglutarate-bound (8SUT)
Data collection			
Space group	$P2_12_12_1$	$P2_12_12_1$	$P2_12_12_1$
Cell dimensions			
a, b, c (Å)	53.94, 93.77, 125.48	52.34, 94.84, 123.94	53.69, 93.98, 124.98
α, β, γ (°)	90.00, 90.00, 90.00	90.00, 90.00, 90.00	90.00, 90.00, 90.00
Resolution (Å)	46.93–2.26 (2.32–2.26)	48.21–2.4 (2.49–2.4)	46.99–1.93 (1.98–1.93)
R_{sym} or R_{merge}	0.117 (2.209)	0.135 (1.46)	0.068 (1.421)
$I/\sigma I$	11.9 (0.7)	14 (1.2)	12.4 (0.7)
Completeness (%)	100 (100)	99 (99.7)	98.2 (83.2)
Redundancy	6.3 (5.5)	11.5 (6.2)	4.6 (3.1)
CC1/2	0.998 (0.298)	0.998 (0.386)	0.998 (0.259)
Refinement			
Resolution (Å)	46.93–2.26	48.21–2.4	46.99–1.93
No. reflections	28,549	24,570	45,270
R_{work}/R_{free}	0.211/0.255	0.189/0.236	0.183/0.23
No. atoms			
Protein	4,500	4,674	4,668
Ligand(s)	2	14	24
Water	50	117	148
B-factors (median)			
Protein	61	45	43
Ligand(s)	101	60.5	64
RMS deviations			
Bond lengths (Å)	0.009	0.008	0.014
Bond angles (°)	1.141	1.171	1.36

[a]Highest resolution shell is shown in parentheses.

Structural characterization of YisK

To investigate YisK's potential catalytic activity and address the possible functional implications for the interaction between YisK and Mbl, we characterized YisK structurally. C-terminally His-tagged YisK was overexpressed and purified, and following screening, initial crystal hits were obtained in the presence of Tacsimate. To optimize the conditions and achieve uniformly liganded protein, we complexed YisK with Mn^{2+} and a subset of the ligands identified in DSF experiments and repeated crystallization condition screening. The newly identified polyethylene glycol (PEG)-based crystallization condition was used for all structures reported in this paper. The structure of YisK in the complex with oxalate (a potent inhibitor of the FAH proteins FADH1 and Cg 1458) (27, 35) and Mn^{2+} was solved at a resolution of 2.4 Å by molecular replacement using a homology model created by Phyre2 (36). YisK crystalized as homodimer with one dimer in the asymmetric unit of a $P2_12_12_1$ crystal lattice. Each subunit is composed of a large and small domain (Fig. 4A and B). The fold of the larger domain is highly conserved among FAH proteins and harbors a triad of negatively charged amino acids (E148, E150, and D179 in YisK) that coordinate a divalent cation typically required for catalysis (25). The smaller domain is variable in size and sequence among the FAH superfamily and often corresponds to a domain of unknown function (DUF2437/PF10370).

A structural similarity search using VAST (37) indicated that YisK shares the highest homology with FAH from mouse (1HYO), 5-carboxymethyl-2-hydroxymuconate delta-isomerase from *Mycobacterium smegmatis* (4PFZ), and HpcE from *Thermus thermophilus* (1WZO), with VAST scores of 39.4, 39.3, and 39, respectively. The root-mean-square deviation (RMSD) calculated for Cα of the YisK large domain superposed with these hits varies between 1.5 and 2.8 Å. The next 18 VAST hits had scores from 23.4 to 38.1, with the similarity driven by the high sequence conservation of the FAH catalytic fold.
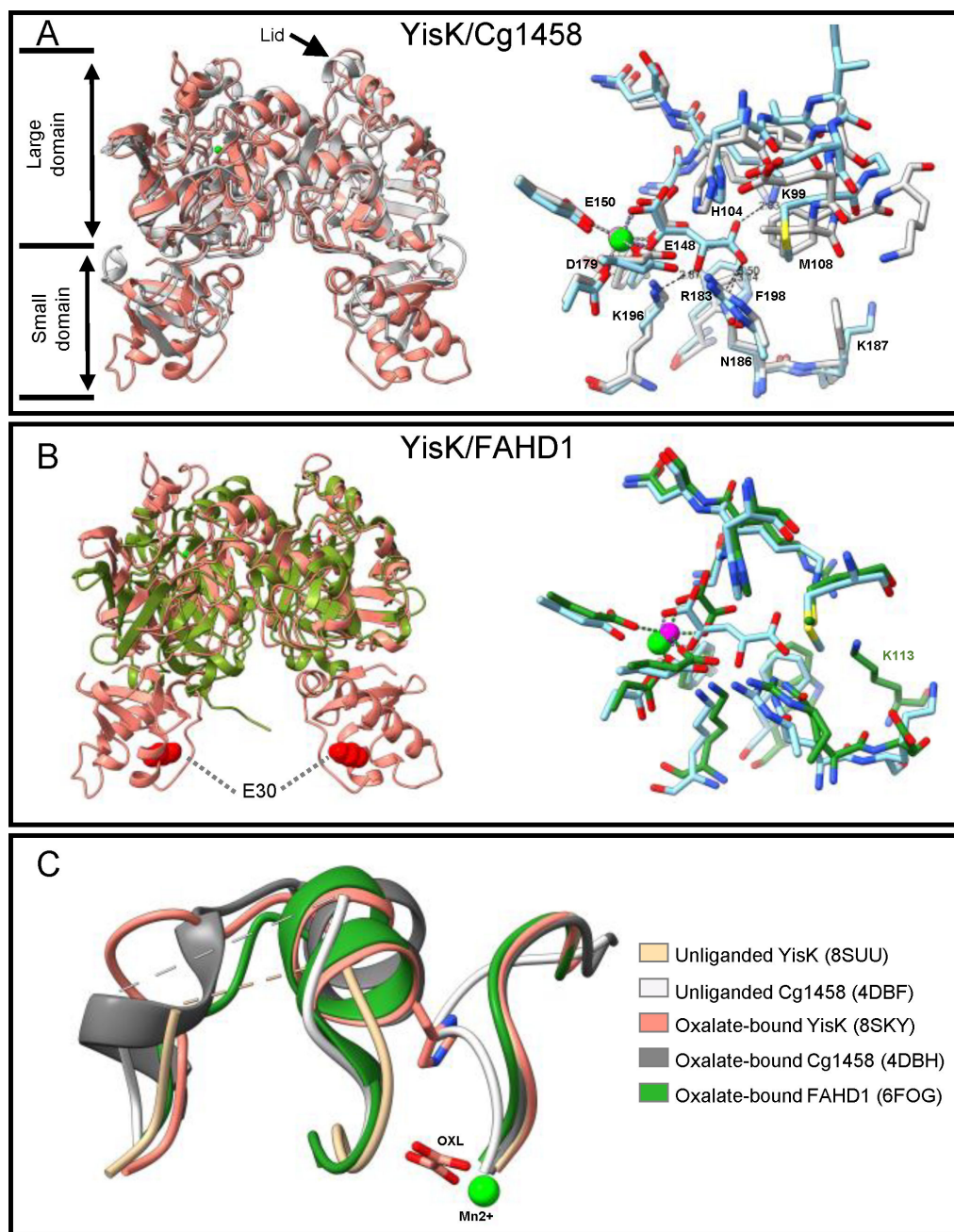
FIG 4 Comparison of YisK structure with the oxaloacetate decarboxylases Cg1458 and FAHD1. (A and B, left) Cartoon representation of YisK dimer (salmon) superimposed with (A) Cg1458 (light gray) and (B) FAHD1 (green). Residue E30 (red spheres) is important for YisK localization and part of the small domain absent in FAHD1. (A and B, right) Active site comparison between 4-hydroxy-2-oxoglutarate-bound YisK (8SUT, light blue carbons) with (A) oxalate-bound Cg1458 (4DBH, light gray carbons) and (B) FAHD1 (6FOG, green carbons). The models are colored by heteroatom. Only the 4-hydroxy-2-oxo-glutarate ligand is shown. Mn^{2+} (green) and Mg^{2+} (magenta) are shown as spheres. (C) Conformational changes between the liganded and unliganded FAH enzyme structures. Unliganded YisK (beige) and Cg1458 (white) with the lids disordered and open, respectively. The oxalate-bound forms of YisK (salmon), Cg1458 (dark gray), and FAHD1 (green) with the lid closed. Disordered segments are depicted as dashed lines. Oxalate (OXL) and YisK's His104 side chain are shown as stick models. The Mn^{2+} (green sphere) is from the YisK structure (8SKY). There is a positional clash between loop 238-242 of the unliganded Cg1458 (white) and His104 of oxalate-bound YisK.

As FAH domain proteins are known to sustain an array of catalytic functions (e.g., hydrolase, decarboxylase, and isomerase), comparing the overall fold of YisK to known FAH family proteins is not very informative for revealing potential catalytic and substrate specificity. Therefore, we instead examined the composition of the active site residues and compared those to homologs, considering not only sequence but also 3D positional alignments. The highest sequence similarity was discovered with two OAA decarboxylases: human mitochondrial FAHD1 with 43% identity over 59% of covered sequence and *Corynebacterium glutamicum* Cg1458 with 36% identity over 74% of covered sequence (Fig. S3A); the RMSDs over the aligned main chain pairs were 0.96 and 0.85 Å, respectively. The overall structures of the large domains are similar, differing only in the small domain (Fig. 4A and B), particularly for FAHD1 in which the small domain is essentially absent (Fig. 4B). In the structures, YisK binds Mn^{2+} while both Cg1458 and FAHD1 bind Mg^{2+}. However, Cg1458 possessed the highest activity *in vitro* with Mn^{2+}-containing buffer (27). The overlay of the ligand-bound FAHD1, Cg1458, and YisK structures (Fig. 4A and B) shows that all of the residues proposed to coordinate the metal and substrate and participate in the catalysis are conserved; this includes the histidine–glutamate–water triad (H104, E148) common among FAH family proteins with carbon–carbon bond cleaving activities (Fig. S3A) (27). Only a few differences occurred in close proximity to the ligand; the K99/F192 equivalent positions of YisK are replaced with R25/W119 in FAHD1 and R68/W160 in Cg1458. In addition, in place of YisK M108 (of the lid) (Fig. S3A), Cg1458 has V77 followed by F78, the latter of which blocks Cg1458's active site due to its bulky sidechain. Additionally, FAHD1 has a short sequence insertion compared to YisK (Fig. S3A), which contributes K113 to the closing of the active site (Fig. 4B). These structural observations led us to hypothesize that YisK can decarboxylate OAA, which was confirmed by a coupled enzyme assay (see below). Given that the differences in YisK make the active site less constricted compared to the other OAA decarboxylases, it is possible that YisK can also accommodate larger substrates.

Prompted by the thermal shift analysis, which identified other potential ligands, we successfully cocrystallized YisK with oxalomalate. We noted that the difference in electron density for the ligand coordinated to Mn^{2+} was consistent with the product of oxalomalate decarboxylation, HOGA (Fig. S3B), suggesting that YisK can decarboxylate other substrates; although we think it is unlikely based on the crystallization conditions, we do not rule out the possibility that the oxalomalate's decarboxylation occurred spontaneously. Regardless, this structure illustrates how a ligand larger than OAA can be accommodated in the YisK active site with the keto-acid moiety stabilized by contacts with N186, R183, and K99, distal to Mn^{2+} (Fig. S3B). The overall protein structure does not differ significantly between oxalate and 4-hydroxy-2-oxoglutarate-bound structures (Fig. S3C).

Interestingly, an analysis of the electron density maps of YisK crystals formed in the presence of OAA revealed an unliganded active site, with only a Mn^{2+} ion coordinated by the protein side chains and water molecules. From this, we think that it is likely that OAA bound to the active site was decarboxylated during crystallization and that the resultant pyruvate lacked sufficient affinity to stay ordered. Consistent with this interpretation, a density for pyruvate was also not observed following crystallization in the presence of high concentrations of pyruvate. The crystals set with OAA produced an effectively "apo" structure of YisK. The open lid conformation signified by the loss of an ordered structure for the residues 105-114 on chain A and 103-–113 on chain B is similar to what was shown for apo Cg1458 and FAHD1 (27, 35). Notably, this transition starts at the catalytic H104, which is still visible on chain A but is a part of the disordered segment on chain B. From this, we infer that ligand binding is the most likely driver of the conformation change resulting in the lid closure and ordering of the 103-114 segment. In contrast to the true apo structure of Cg1458, we do not observe in our apparent apo YisK structure the transition equivalent to Cg1458 loop 238-242, which takes the place of the lid residues' side chains, including the catalytic histidine of the liganded structure conformation (Fig. 4C). Although this segment is relatively conserved by sequence

(SPAGT in Cg1458 versus TPSGV in YisK), in YisK, it is followed by a seven-amino acid-long insertion (Fig. S3A) that may affect the mobility of the neighboring loop. Like YisK, the unliganded FAHD1 structure (6FOH) does not show the movement of an analogous loop (Fig. 4C). Hence, loop 238-242 blocking the active site conformation state may be unique to Cg1458; it is also possible that the way we obtained the unliganded structure of YisK (through dissociation of the reaction product) did not allow for this conformation.

YisK protein can catalyze the decarboxylation of OAA to pyruvate and CO_2

Although we identified several chemical features YisK's substrate(s) is/are likely to possess (Fig. 3F), the number of potential substrates remained large. A comparison of the YisK structure with the crystal structures of other FAH family proteins revealed strong active site similarity with two OAA decarboxylases, FAHD1 and Cg1458 (Fig. 4A and B). To test if YisK also has OAA decarboxylase activity, we performed a coupled lactate dehydrogenase assay, monitoring the conversion of pyruvate to lactate spectrophotometrically by following the oxidation of NADH to NAD+ at 340 nm. OAA spontaneously decarboxylates in the solution (Fig. 5A) (38, 39), so the apparent kinetic constants for YisK-catalyzed OAA decarboxylation were determined after subtracting the rate of spontaneous decarboxylation (Fig. 5A) that occurred in the absence of YisK. The YisK-catalyzed reaction rate was plotted (Fig. 5B) and used to derive the following apparent kinetic constants: k_{cat}: 0.52 ± 0.02 s^{-1}, K_m: 134 ± 22 µM, and k_{cat}/K_m: 3.8 × 10^3 M^{-1} s^{-1}.

As a control, the assay was also performed with the YisK E148A E150A variant that is predicted to be catalytically dead due to the loss of the Mn^{2+} cofactor. As expected, YisK E148A E150A had no detectable activity (Fig. 5B). In contrast, introducing a substitution in the small domain distal to the active site (YisK E30A) (Fig. 4B) had no effect on catalytic activity (Fig. 5B). These data support the idea that YisK-dependent OAA decarboxylation requires the metal cofactor and exclude the possibility that the observed activity is due to either spontaneous decarboxylation or another enzyme contaminating the protein preparation. We conclude that YisK possesses OAA decarboxylase activity.

Catalytically inactivated YisK can still widen cells and exhibit wild-type localization

To test whether YisK's enzymatic activity is required for the overexpression phenotypes, we placed YisK E148A E150A under the control of an IPTG-inducible promoter. Following induction, the catalytic dead variant still prevented growth on LB plates and led to the loss of control over cell dimensions in liquid LB (Fig. 6A). Moreover, a GFP fused version of YisK E148A E150A expressed from the native locus still exhibited punctate localization (Fig. 6B). These results indicate that YisK's localization and interaction with the elongasome do not depend on its catalytic activity. In addition, since YisK E148 E150A is unlikely to efficiently bind ligands (Fig. 5G), the results also suggest that YisK's punctate localization is not dependent on ligand binding.

YisK E30A localizes diffusely and does not perturb growth following overexpression

Prior to solving the crystal structure, we identified a small cluster of charged residues (EKK) in the small domain of YisK that we predicted might be surface-exposed. We hypothesized that this region of YisK might be important for protein–protein interaction and/or localization and generated a YisK E30A substitution to assay for functionality. In contrast to wild-type YisK, the overexpression of YisK E30A did not prevent growth or cause cell widening (Fig. 6C). YisK E30A expression was indistinguishable from wild-type YisK by western blot analysis (Fig. 6D), suggesting that the loss-of-function phenotypes were not attributable to a problem with protein expression. Moreover, YisK E30A maintained wild-type self-interaction in a bacterial two-hybrid assay (Fig. 6E) and exhibited wild-type enzymatic activity *in vitro* (Fig. 5B), both consistent with proper

A

$$Y_{spon} = 6.69 \times 10^{-5} \times [S]$$

B

WT:
kcat: 0.52 ± 0.02 s^{-1}
Km: 134 ± 22 μM
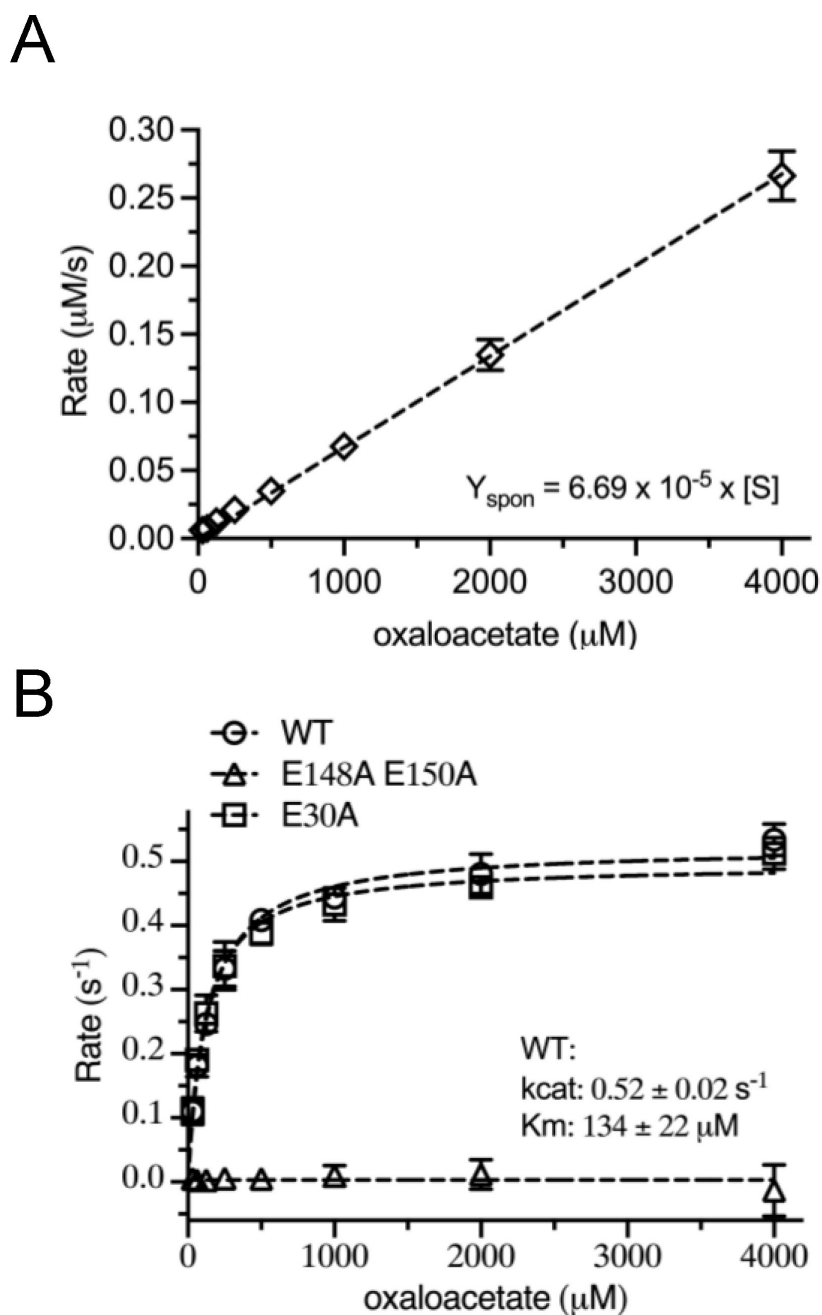
FIG 5 Coupled assay to detect oxaloacetate decarboxylase activity. (A) Spontaneous decarboxylation of oxaloacetate at 25°C in buffer containing 0.3 mM NADH, 1.0 unit lactate dehydrogenase, and the indicated concentration of oxaloacetate. The dashed line represents the linear fits for the data. (B) Michaelis–Menten plot for decarboxylation of oxaloacetate catalyzed by YisK and variants after subtracting spontaneous decarboxylation. Reactions were carried out at 25°C in buffer containing 0.3 mM NADH, 1.0 unit lactate dehydrogenase, and the indicated concentration of oxaloacetate and initiated by the addition of 0.5 μM YisK. The dashed line represents the fit of the data to $v/E_t = \kappa_{cat}(S)/(\kappa_m + S)$.

folding. Strikingly, YisK$_{SW}$-GFP E30A expressed from YisK's native promoter exhibited only diffuse localization (Fig. 6B). These results suggest that the small domain is important for YisK's Mbl-dependent punctate localization and ability to perturb Mbl function.
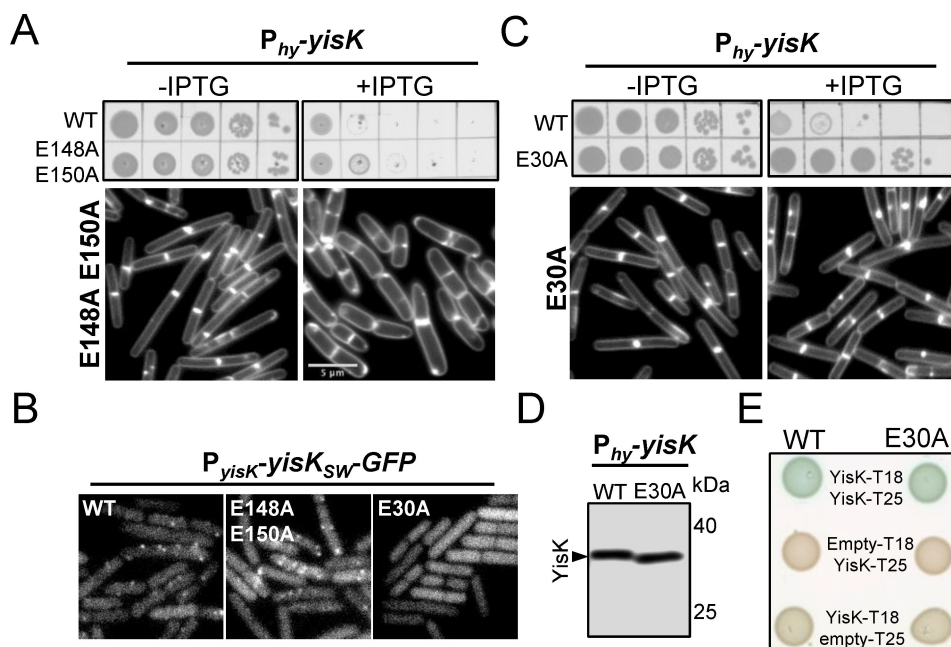
FIG 6 YisK variant overexpression phenotypes and localization. (A and C) Growth of cells harboring indicated construct after overnight incubation (top) and following 90-min overexpression in LB-Mg (bottom). Membranes are stained with TMA and shown at the same magnification. (B) Representative micrographs showing localization of the indicated YisK$_{SW}$-GFP variants following 60-min growth in sporulation by resuspension medium (native promoter). Images are of the same magnification and scaled identically in the GFP channel. (D) Western blot analysis of samples collected from cells harboring wild-type P_{hy}-yisK and P_{hy}-yisK E30A following 60-min induction. (E) Bacterial two-hybrid analysis of YisK self-interaction.

DISCUSSION

Is OAA YisK's preferred substrate?

The YisK-catalyzed turnover of OAA was 31 min^{-1}, rather slow for a typical enzyme. We can envision several possible explanations for the modest turnover. First, it is entirely possible that OAA is not a preferred substrate. If so, additional testing may eventually lead to better candidates. Second, assuming an intracellular OAA concentration of 0.5 µM (the estimate for *Escherichia coli*) (40), YisK-catalyzed decarboxylation would be around 30 times faster than the spontaneous rate observed in our reaction buffer (Fig. 5A). This degree of catalytic enhancement could conceivably be sufficient for the cell's needs, especially considering that YisK is a relatively abundant protein (21, 23). Third, YisK's punctate localization suggests the enzyme may reach high concentrations locally, which could be important for *in vivo* activity; relatedly, the *in vitro* assay may lack one or more factors that enhance YisK activity, such as an interaction partner. Finally, YisK could function more as a metabolite sensor than an enzyme. For example, upon ligand binding (or release), YisK could adjust some activity related to elongasome function. YisK likely does not require a ligand to localize, as the variant with low affinity for ligands (YisK E148A E150A) (Fig. 3G) and no detectable enzymatic activity (Fig. 5B) can still form puncta and widen cells (Fig. 6A and B); at the same time, our data do not rule out the possibility that ligand binding could cause YisK to delocalize and/or change its function.

OAA is an important metabolic intermediate that, along with phosphoenolpyruvate and pyruvate, forms the central node connecting glycolysis, gluconeogenesis, and the TCA cycle (41, 42). It is also the precursor to aspartate, the aspartate-derived amino acids asparagine, methionine, threonine, isoleucine, and lysine, and in bacteria, the PG precursor meso-diaminopimelic acid. OAA is also a potent inhibitor of succinate dehydrogenase (43–47), and control of OAA levels is proposed to be integral to TCA cycle regulation and electron transport chain function (48, 49). The inhibition of succinate

dehydrogenase by OAA leads to a drop in proton motive force and ATP synthesis and also reduces oxidative stress (50). The depletion of mitochondrial FAHD1 in human epithelial cell lines disrupts electron transport chain function and triggers senescence, and it has been proposed that FAHD1 may play a role in TCA cycle regulation (51). If YisK functions as an OAA decarboxylase *in vivo*, then it could also buffer the cell against succinate dehydrogenase inhibition. Notably, YisK protein accumulates to the highest levels when carbon or nitrogen sources become limited (23, 52, 53) and after cells exit exponential growth (Fig. 1; Fig. S1). As this is also when the punctate localization becomes most evident, it is of considerable interest to learn if the foci have more, less, or the same level of enzymatic activity as the diffuse protein.

YisK localization

The catalytic dead variant, YisK E148A E150A, retains punctate localization (Fig. 6B) and still widens cells when overexpressed (Fig. 6A). Conversely, cells are insensitive to the overexpression of the YisK E30A variant, which possesses wild-type enzymatic activity (Fig. 5B) but localizes only diffusely (Fig. 6B). Notably, the Δ*ponA* Δ*mbl* background, which is also resistant to YisK overexpression (19), similarly supports only diffuse localization (Fig. 2D; Fig. S2A). Although a direct interaction between YisK and Mbl would explain both YisK's dependence on Mbl for localization and its overexpression phenotypes (19), we currently lack evidence supporting this model.

The small domain of YisK is structurally unique, as a VAST search identified only limited structural similarity for regions 1-29 and 74-82 that together constitute part of a domain of unknown function frequently fused to the N-terminus of FAH-like proteins; addressing the small domain's role in YisK function could also inform our understanding of this uncharacterized protein fold. In contrast, region 30-73 had no structurally similar hits in the Protein Data Bank. Remarkably, a single substitution in the small domain (E30A) completely abolished the formation of YisK's Mbl-dependent foci, suggesting that this region of YisK likely constitutes part of a localization domain. The localization of the catalytically inactive mutant (E148A, E150A) was indistinguishable from that of wild-type YisK (Fig. 6B). Consistent with this observation, no significant conformational changes were detected in the small domain between the ligand-bound and apo states (Fig. S3C). At the same time, we do not exclude the possibility that the ligand-dependent conformational change in the lid region of YisK could be coupled to the regulation of another partner and/or binding event.

We are left with the question as to why an enzyme implicated in central carbon metabolism would not only exhibit subcellular localization but also evolve associations with components of the envelope synthesis machinery. There is evidence of higher-order associations among the TCA cycle enzymes (54) and precedence for functional interactions between metabolic enzymes and the cell division protein FtsZ (55–58). To our knowledge, YisK is the first example of an enzyme not obviously linked to envelope synthesis that depends on Mbl for localization. YisK's interaction with the elongasome could be a means for the cell to couple central carbon metabolism with envelope synthesis and/or degradation. Alternatively, YisK may possess an enzymatic activity or regulatory role more directly related to cell wall synthesis or turnover. Future experiments will aim to address the functional significance of YisK's interaction with the elongasome.

MATERIALS AND METHODS

General methods

Details of strain construction can be found in the Supplementary Materials. Cells were stored at −80°C in 15.0% glycerol (vol/vol). All LB is Lysogeny Broth–Lennox. Strains were streaked for isolation on LB plates containing 1.5% (wt/vol) bacto agar and incubated overnight (~16 hr) at 37°C. Cultures for experiments were started from same-day plates

by inoculating single colonies into 20-mm glass tubes containing 5.0 mL of medium indicated in the associated figure. The tubes were incubated at 37°C in a roller drum until the exponential stage. For experiments, the exponential pre-cultures were used to inoculate 25.0 mL of medium in a 250-mL baffled flask. Cells were incubated in a shaking water bath set to 280 rpm and 37°C.

Liquid LB was made by dissolving 20.0 g of LB–Lennox powder (Difco, product #240230) in 1.0-L ddH$_2$O, followed by sterilization in an autoclave. LB-Mg indicates LB supplemented with 10.0-mM MgCl$_2$. Each 1.0 L of CH medium (59) contained 10.0-g casein acid hydrolysate (Acumedia, Lot No. 104,442B), 3.7-g L-glutamic acid (25.0 mM), 1.6-g L-asparagine monohydrate (10.0 mM), 1.25-g L-alanine (14.0 mM), 1.36-g (10.0 mM) KH$_2$PO$_4$ anhydrous, 1.34-g (25.0 mM) NH$_4$Cl, 0.11-g Na$_2$SO$_4$ (0.77 mM), 0.1-g NH$_4$NO$_3$ (1.25 mM), and 0.001-g FeCl$_3$·6H$_2$O (3.7 mM) and ddH$_2$O. The pH was adjusted to 7.0 with 10.0 N NaOH before the volume was brought up to 1.0 L with ddH$_2$O, and the medium was sterilized in an autoclave. After autoclaving, sterilized solutions were added to give the following final concentrations: 0.18 mM CaCl$_2$, 0.4 mM MgSO$_4$, 0.1 mM MnSO$_4$, and 0.1 mM L-tryptophan. Sporulation by resuspension medium was made as described (59).

Plate growth assays

B. subtilis strains were cultured in a 5.0-mL LB tube on the roller drum at 37°C to OD$_{600}$ ~0.5. Then, cells are back-diluted in LB to OD$_{600}$ 0.1, 0.01, 0.001, 0.0001, and 0.00001. Five microliters of each sample is spotted on LB–Lennox plates containing 100.0 µg/mL spectinomycin without and with 1.0-mM IPTG, respectively. Plates were incubated at 37°C overnight, and images were captured on a Scanjet G4050 flatbed scanner (Hewlett Packard).

Bacterial two-hybrid analysis

Bacterial two-hybrid analysis was performed as described (60) with the following modifications: cloning was carried out in the presence of 0.2% glucose. Cells harboring the relevant pairwise interactions were grown to the early exponential phase in LB with 0.2% glucose, 50.0 µg/mL ampicillin, and 25.0 µg/mL kanamycin. Samples were spotted to an OD$_{600}$ of 0.1 and 5.0 µL of each culture on M9-glucose minimal media plates containing 40.0 µg/mL 5-bromo-4-chloro-3-indolyl-β-D-galactopyranoside, 250.0 µM IPTG, 50.0 µg/mL ampicillin, and 25.0 µg/mL kanamycin. Plates were incubated at 37°C in the dark for 20 hr for color development prior to image capture.

Western blot analysis

Cultures were grown to the exponential stage, and 1 mL of culture was collected and spun at 21,130 × *g* for 1 min at room temperature. The OD$_{600}$ value at the time of sampling was recorded. The pellet was resuspended in the lysis buffer [20.0 mM Tris, pH 7.5, 10.0 mM EDTA, 1.0 mg/mL lysozyme, 10.0 µg/mL DNase I, 100.0 µg/mL RNase A, 1.0 mM PMSF, 1 µL protease inhibitor cocktail (Sigma P8465-5ML)] to give a final OD$_{600}$ equivalent of 15. The samples were incubated at 37°C for 10 min followed by the addition of an equal volume of sodium dodecyl sulfate (SDS) sample buffer [0.25 M Tris, pH 6.8, 4% (wt/vol), 20% (wt/vol) SDS, 20% (vol/vol) glycerol, 10.0 mM EDTA, and 10% (vol/vol) β-mercaptoethanol]. Samples were boiled for 5 min prior to loading. Proteins were separated on 12% SDS-PAGE polyacrylamide gels and transferred to a nitrocellulose membrane at 100 V for 60 min. The membrane was blocked in 1× PBS containing 0.05% (vol/vol) Tween-20 and 5% (wt/vol) dry milk powder. The blocked membranes were then probed overnight at 4°C with anti-YisK antibody (1:10,000, rabbit serum) diluted in 1× PBS with 0.05% (vol/vol) Tween-20 and 5% (wt/vol) milk powder. The membranes were washed three times with 1× PBS containing 0.05% (vol/vol) Tween-20 before transferring to 1× PBS with 0.05% (vol/vol) Tween-20 and 5% (wt/vol) milk powder containing 1:5,000 horseradish peroxidase-conjugated goat anti-rabbit IgG secondary antibody (Rockland 611-1302) and incubated on a shaking platform for 1 hr at room temperature. The

membranes were washed 3× with PBS containing 0.05% (vol/vol) Tween-20, and the signal was detected using the SuperSignal West Femto maximum sensitivity substrate (Thermo Fisher) and a Bio-Rad Gel Doc Imaging System.

Fluorescence microscopy

For microscopy experiments, all strains were grown in the indicated medium in volumes of 25.0 mL in 250-mL baffled flasks and placed in a shaking water bath set at 37°C and 280 rpm. Unless stated otherwise, overexpression was performed in LB-Mg by inducing samples with 1.0 mM IPTG. Cells were always imaged below an OD_{600} of 0.7. Sporulation was performed by growing cells in the CH medium (59) followed by resuspension in the sporulation medium (59, 61). To capture images of membranes, 1 mL of cultured cells was harvested and concentrated by centrifugation at $6,010 \times g$ for 1 min and resuspended in 5.0 µL 1× PBS with TMA-DPH (50.0 µM). Cells were mounted on glass sides with polylysine-treated coverslips prior to imaging. For the YisK-GFP experiments, cells were mounted on 1% (wt/vol) agarose pads made with ddH_2O and overlaid with a coverslip. Cells were imaged on a Nikon Ti-E microscope with a CFI Plan Apo Lambda DM 100× objective and Prior Scientific Lumen 200 illumination system. The filter cubes utilized were C-FL UV-2E/C (TMA), HC HISN Zero Shift (GFP) filter cubes. Micrographs were acquired with a CoolSNAP HQ2 monochrome camera using NIS-Elements Advanced Research and processed in NIS-Elements or ImageJ (62).

Protein purification

Wild-type YisK, YisK E30A, and YisK E148A E150A were expressed as C-terminal histidine tag fusions (strain construction in the Supplementary Materials) by transforming competent BL21(λDE3)pLysS cells with the pET24b-based plasmids and selecting on LB agar plates supplemented with 25.0-µg/mL kanamycin. Following overnight growth at 37°C, colonies were aseptically scraped from the plate and resuspended in 5.0 mL of Cinnabar medium (Teknova). This suspension was used to inoculate a 250-mL baffled flask containing 25.0 mL Cinnabar supplemented with 0.1% (wt/vol) glucose and 25.0 µg/mL kanamycin to a starting OD_{600} of 0.1. Cultures were grown in shaking waterbath (250–280 rpm) at 37°C until culture reached an OD_{600} of approximately five at which point IPTG was added to 1.0 mM. The culture was then placed in a 16°C shaker overnight (~16 hr). The cells were collected by centrifuging at $8,000 \times g$ for 10 min at 4°C. The supernatant was aspirated, and the pellets were frozen at −80°C. To purify the protein, the pellet was resuspended in 25.0 mL lysis buffer (50.0 mM Tris-HCl [pH 8.0], 300.0 mM NaCl, 10.0 mM imidazole, 10% (vol/vol) glycerol, 200 µg/mL lysozyme, 10.0 µg/mL DNase, 1.0 µL per 35 OD*mL protease inhibitor cocktail (Sigma P8465), and 0.5 mL 100.0 mM phenylmethylsulphonyl fluoride] and lysed using a LM20 Microfluidizer (Microfluidics) at 20,000 psi. Cell debris was removed by centrifugation at $41,656 \times g$ for 30 min at 4°C.

The supernatant was collected and, at room temperature, was passed over a 2.0 mL bed volume of Ni-NTA Sepharose resin (Qiagen). The column was then washed three times with 10.0 mL of wash buffer [50.0 mM Tris-HCl (pH 8.0), 300.0 mM NaCl, 25.0 mM imidazole, and 10% (vol/vol) glycerol]. Elutions were carried out with 12 × 0.5 mL of elution buffer [50.0 mM Tris-HCl (pH 8.0), 300.0 mM NaCl, 10% (vol/vol) glycerol] and 300.0 mM imidazole. Fractions containing the protein were pooled and dialyzed against 20.0 mM HEPES (pH 7.5), 150.0 mM NaCl, 15% (vol/vol) glycerol, and 2.0 mM DTT and frozen as aliquots at −80°C. These protein stocks were used in the differential scanning fluorimetry and enzyme activity assays. Protein purified for crystallization was dialyzed against 50.0 mM Tris-HCl (pH 7.5) and 1.0 mM DTT and used immediately.

YisK crystallization

Five hundred eighty-six separate crystallization conditions were screened in a 96-well plate using a TTP LabTech Mosquito LCP machine. Initial crystals were obtained in 60%

Tacsimate (Hampton Research) (pH 7.5) and 10% Tacsimate (Hampton Research) (pH 5.0), 20% (wt/vol) PEG 2000 with various divalent cations. Optimized conditions used YisK-6His at 12.0 mg/mL (by Bradford assay) in buffer containing 50.0 mM Tris (pH 7.5) and 1.0 mM DTT set in a 1:1 vol ratio and 2:1 ratio with mother liquor [60% Tacsimate (pH 7.0), 100.0 mM $MnCl_2$]. The initial solution based on these crystals indicated dicarboxylic components from Tacsimate binding in the active site. To find Tacsimate-free crystallization conditions, we pre-made YisK as a complex with Mn^{2+} and oxalate (at 3.0 mM final concentration) and repeated crystal screening. PEG-based crystal hit conditions were chosen for subsequent optimization. Oxaloacetate-complexed YisK, which resulted in an apparent apo structure, and oxalomalate-complexed YisK, which resulted in a HOGA-bound structure, were crystallized with mother liquor of 0.2 M Mg-acetate and 20% (wt/vol) PEG 3350. Oxalate-bound YisK was crystallized with 0.1 M AmSO4, 25% (wt/vol) PEG 4000 and 15% (vol/vol) glycerol. All crystals were cryoprotected by adding glycerol to the corresponding mother liquor to the final concentration of 30% (vol/vol) and flash-frozen in a liquid nitrogen for the data collection.

Data collection and analysis

The oxalate-bound structure was solved from the crystal collected at BL502 beamline of Lawrence Berkeley National Lab synchrotron; two other structures resulted from the data collected at 23ID beamline of Argonne National Lab synchrotron. Data were indexed, integrated, and scaled by the beamline auto-processing pipeline: XDS (63), POINTLESS (64), and AIMLESS (65) software packages. The structure was solved by molecular replacement with Molrep software (66) using a manually edited Phyre2 generated homology model as a search model for the first solution. This was followed by iterative cycles of refinement with PHENIX.REFINE and manual building in COOT (67, 68). A ligand model and restraints were created using the eLBOW tool (69). The initial solution showed poor refinement R factors, and upon examination of the electron density maps, it became evident that while the larger catalytic domain refined well to the homology model, the smaller domain was substantially different both in fold and position relative to the main domain. The smaller domain was fully rebuilt through stepwise iterative building and refinement cycles. The data collection and refinement statistics are shown in Table 1.

Differential scanning fluorimetry (thermal shift assays)

Differential scanning fluorimetry was performed as previously (70), with minor modifications. In the screen for stabilizing molecules, a master mix of either 1.0 or 10.0 μM YisK-His (concentration indicated in the table legend) in 20.0 mM HEPES (pH 7.5), 150.0 mM NaCl, and 5.0 mM $MnCl_2$ or, when indicated in the table legend, 1.0 mM $MnCl_2$, 1.0 mM $MgCl_2$, and 1.0 mM $CaCl_2$ was made, including 5× Sypro Orange. The 5,000× Sypro Orange was added to master mix before YisK-His to avoid possible effects of the concentrated Sypro Orange solvent. Thirty-nine microliters of the master mix was aliquoted into each well on a Bio-Rad Hard-Shell PCR Plates, 96-well format, thin wall (HSP9601). To each well, 1.0 μL of compound was added to give a final concentration of 1.0 mM. Reactions were mixed by repeated pipetting after adding the compound. The PCR plate was then sealed with the Bio-Rad Microseal 'B' seal (MSB1001) and centrifuged at $1,000 \times g$ for 3 min in a centrifuge equipped with a plate adaptor at RT to remove bubbles. The plate was placed in a CFX96 Touch Real-Time PCR machine running a custom program as follows: initial temperature, 25°C ramped to 95°C at a rate of 0.5°C/min, acquiring the signal from the FRET channel. The final data were analyzed using the Bio-Rad CFX Manager, with the baseline subtracted curve fit analysis mode. The derivative of the melting curve was used to determine the melting temperature of YisK in all assayed conditions.

To assay for apparent metal binding affinity, a master mix of 10.0 μM YisK-His in 20.0 mM HEPES (pH 7.5), 150 mM NaCl, 5× Sypro Orange was made with gradient $MnCl_2$

or MgCl$_2$. Thirty-nine microliters of this master mix was aliquoted into each well on Bio-Rad Hard-Shell PCR Plates, 96-well format, thin wall (HSP9601). To each well, either 1.0 µL of reaction buffer alone (20.0 mM HEPES, pH 7.5, 150 mM NaCl) or 1.0 µL of MnCl$_2$ or MgCl$_2$ was added to give the final gradient concentration indicated in the figures. The samples were then processed as described for the compound screen.

Determination of kinetic constants

The kinetic constants for YisK were determined by following the conversion of NADH to NAD$^+$ at 340 nm at 25℃ with a SpectraMax 340 UV-visible spectrophotometer. Assays were performed in 50.0 mM HEPES (pH 7.5), 150.0 mM NaCl, 1.0 mM MnCl$_2$, 0.3 mM NADH, and 1 unit of lactate dehydrogenase in 96-well NucC plates. The spontaneous rate of decarboxylation was monitored in buffer containing all but the addition of YisK. The reactions with YisK were initiated with the addition of 0.5 µM protein to the reaction well. Kinetic constants were determined with variable levels of OAA (0.031–4.0 mM). The kinetic parameters were determined by fitting the initial rates to the equation $v/E_t = \kappa_{cat}(S)/(\kappa_m + S)$ using Prism 9 graph, where v is the initial velocity of the reaction, E_t is the enzyme concentration, k_{cat} is the turnover number, $[S]$ is the substrate concentration, and K_m is the Michaelis constant.

Statistical analysis and data plotting

Graphs were generated, and statistical analysis was performed using GraphPad Prism version 9.4.0 for Mac (GraphPad Software, San Diego, CA, USA; www.graphpad.com).

Whole-genome sequencing and analysis

Single colonies of Δ$ponA$* (BYD172) and Δ$ponA$ (BYD048) were inoculated into 5.0 mL LB-Mg and grown at 37℃ for 4 hr in a roller drum. One milliliter of cells was collected by centrifuging at 21,130 × g (room temperature) for 2 min, then aspirating the supernatant. Pellets were resuspended in lysis buffer [20.0 mM Tris-HCl, pH 7.5, 50.0 mM EDTA (pH 8.0), 100.0 mM NaCl, and 2.0 mg/mL lysozyme] and incubated at 37℃ for 30 min before sarkosyl was added to a final concentration of 1.0% (wt/vol). Protein was extracted with 600 µL phenol by vortexing the lysate and phenol before centrifuging at 21,130 × g for 5 min at room temperature. The aqueous layer (top) was transferred to a new microcentrifuge tube. This was followed by an extraction with 600 µL phenol-saturated chloroform as described above. After transferring the aqueous layer to a new microcentrifuge tube, a final extraction was performed with 100% chloroform, being careful to avoid the interphase material. To precipitate the genomic DNA, a 1/10th volume of 3.0 M Na-acetate and 1.0 mL of 100% ethanol was added, and the tube was inverted multiple times. The sample was centrifuged at 21,130 × g for 1 min at room temperature, and the pellet was washed with 150 µL 70% (vol/vol) ethanol before being resuspended in 500 µL TE [10.0 mM Tris (pH 7.5), 1.0 mM EDTA (pH 8.0)]. To eliminate potential RNA contamination, RNase was added to a final concentration of 200 µg/mL, and the sample was incubated at 55℃ for 1 hr. To remove the RNase, the genomic DNA was repurified by phenol–chloroform and chloroform extraction with ethanol precipitation as described above. The final pellet was resuspended in 100 µL TE buffer. Bar-coded libraries were prepared from each genomic DNA sample using a TruSeq DNA kit according to manufacturer specifications (Illumina), and the samples were subjected to Illumina-based whole-genome sequencing using a MiSeq 250 paired-end run (Illumina). CLC Genomics Workbench (Qiagen) was used to map the sequence reads against the *Bacillus subtilis* 168 reference genome, and single-nucleotide polymorphisms, insertions, and deletions were identified.

AUTHOR AFFILIATIONS

[1]Department of Biochemistry and Biophysics, Texas A&M University, College Station, Texas, USA

[2]Department of Chemistry, Texas A&M University, College Station, Texas, USA

AUTHOR ORCIDs

Jennifer K. Herman http://orcid.org/0000-0003-4100-8167

AUTHOR CONTRIBUTIONS

Tingfeng Guo, Conceptualization, Data curation, Formal analysis, Investigation, Methodology, Validation, Visualization, Writing – original draft, Writing – review and editing | Anthony M. Sperber, Conceptualization, Data curation, Formal analysis, Investigation, Methodology, Validation, Writing – review and editing | Inna V. Krieger, Conceptualization, Data curation, Formal analysis, Investigation, Methodology, Supervision, Validation, Visualization, Writing – original draft, Writing – review and editing | Yi Duan, Conceptualization, Data curation, Formal analysis, Investigation, Methodology, Validation, Writing – review and editing | Veronica R. Chemelewski, Data curation, Formal analysis, Investigation, Methodology, Writing – review and editing | James C. Sacchettini, Conceptualization, Formal analysis, Methodology, Supervision, Writing – review and editing | Jennifer K. Herman, Conceptualization, Data curation, Formal analysis, Funding acquisition, Investigation, Methodology, Project administration, Resources, Supervision, Validation, Visualization, Writing – original draft, Writing – review and editing

ADDITIONAL FILES

The following material is available online.

Supplemental Material

Supplemental material (JB00202-23-s0001.pdf). Fig. S1 to S5, Tables S1 to S4, and Text S1.

REFERENCES

1. Bhavsar AP, Brown ED. 2006. Cell wall assembly in *Bacillus subtilis*: how spirals and spaces challenge paradigms. Mol Microbiol 60:1077–1090. https://doi.org/10.1111/j.1365-2958.2006.05169.x

2. Dover RS, Bitler A, Shimoni E, Trieu-Cuot P, Shai Y. 2015. Multiparametric AFM reveals turgor-responsive net-like peptidoglycan architecture in live streptococci. Nat Commun 6:7193. https://doi.org/10.1038/ncomms8193

3. Gumbart JC, Beeby M, Jensen GJ, Roux B. 2014. *Escherichia coli* peptidoglycan structure and mechanics as predicted by atomic-scale simulations. PLoS Comput Biol 10:e1003475. https://doi.org/10.1371/journal.pcbi.1003475

4. Thwaites JJ, Mendelson NH. 1989. Mechanical properties of peptidoglycan as determined from bacterial thread. Int J Biol Macromol 11:201–206. https://doi.org/10.1016/0141-8130(89)90069-x

5. Vollmer W, Seligman SJ. 2010. Architecture of peptidoglycan: more data and more models. Trends Microbiol 18:59–66. https://doi.org/10.1016/j.tim.2009.12.004

6. Marvasi M, Visscher PT, Casillas Martinez L. 2010. Exopolymeric substances (EPS) from *Bacillus subtilis*: polymers and genes encoding their synthesis. FEMS Microbiol Lett 313:1–9. https://doi.org/10.1111/j.1574-6968.2010.02085.x

7. Angeles DM, Scheffers DJ. 2021. The cell wall of *Bacillus subtilis*. Curr Issues Mol Biol 41:539–596. https://doi.org/10.21775/cimb.041.539

8. Egan AJF, Errington J, Vollmer W. 2020. Regulation of peptidoglycan synthesis and remodelling. Nat Rev Microbiol 18:446–460. https://doi.org/10.1038/s41579-020-0366-3

9. Errington J, Wu LJ. 2017. Cell cycle machinery in *Bacillus subtilis*. Subcell Biochem 84:67–101. https://doi.org/10.1007/978-3-319-53047-5_3

10. Leaver M, Errington J. 2005. Roles for MreC and MreD proteins in helical growth of the cylindrical cell wall in *Bacillus subtilis*. Mol Microbiol 57:1196–1209. https://doi.org/10.1111/j.1365-2958.2005.04736.x

11. Kawai Y, Daniel RA, Errington J. 2009. Regulation of cell wall morphogenesis in *Bacillus subtilis* by recruitment of PBP1 to the MreB helix. Mol Microbiol 71:1131–1144. https://doi.org/10.1111/j.1365-2958.2009.06601.x

12. Kawai Y, Asai K, Errington J. 2009. Partial functional redundancy of MreB isoforms, MreB, Mbl and MreBH, in cell morphogenesis of *Bacillus subtilis*. Mol Microbiol 73:719–731. https://doi.org/10.1111/j.1365-2958.2009.06805.x

13. Mirouze N, Ferret C, Yao Z, Chastanet A, Carballido-López R. 2015. MreB-dependent inhibition of cell elongation during the escape from competence in *Bacillus subtilis*. PLoS Genet 11:e1005299. https://doi.org/10.1371/journal.pgen.1005299

14. Carballido-López R, Formstone A, Li Y, Ehrlich SD, Noirot P, Errington J. 2006. Actin homolog MreBH governs cell morphogenesis by localization of the cell wall hydrolase LytE. Dev Cell 11:399–409. https://doi.org/10.1016/j.devcel.2006.07.017

15. Patel Y, Zhao H, Helmann JD. 2020. A regulatory pathway that selectively up-regulates elongasome function in the absence of class A PBPs. Elife 9:e57902. https://doi.org/10.7554/eLife.57902

16. Domínguez-Cuevas P, Porcelli I, Daniel RA, Errington J. 2013. Differentiated roles for MreB-actin isologues and autolytic enzymes in *Bacillus subtilis* morphogenesis. Mol Microbiol 89:1084–1098. https://doi.org/10.1111/mmi.12335

17. Meisner J, Montero Llopis P, Sham L-T, Garner E, Bernhardt TG, Rudner DZ. 2013. FtsEX is required for CwlO peptidoglycan hydrolase activity during cell wall elongation in *Bacillus subtilis*. Mol Microbiol 89:1069–1083. https://doi.org/10.1111/mmi.12330

18. Brunet YR, Wang X, Rudner DZ. 2019. SweC and SweD are essential cofactors of the FtsEX-CwlO cell wall hydrolase complex in *Bacillus subtilis*. PLoS Genet 15:e1008296. https://doi.org/10.1371/journal.pgen.1008296

19. Duan Y, Sperber AM, Herman JK. 2016. YodL and YisK possess shape-modifying activities that are suppressed by mutations in *Bacillus subtilis* mreB and mbl. J Bacteriol 198:2074–2088. https://doi.org/10.1128/JB.00183-16

20. Britton RA, Eichenberger P, Gonzalez-Pastor JE, Fawcett P, Monson R, Losick R, Grossman AD. 2002. Genome-wide analysis of the stationary-phase sigma factor (sigma-H) regulon of *Bacillus subtilis*. J Bacteriol 184:4881–4890. https://doi.org/10.1128/JB.184.17.4881-4890.2002

21. Tam LT, Antelmann H, Eymann C, Albrecht D, Bernhardt J, Hecker M. 2006. Proteome signatures for stress and starvation in *Bacillus subtilis* as revealed by a 2-D gel image color coding approach. Proteomics 6:4565–4585. https://doi.org/10.1002/pmic.200600100

22. Nicolas P, Mäder U, Dervyn E, Rochat T, Leduc A, Pigeonneau N, Bidnenko E, Marchadier E, Hoebeke M, Aymerich S, et al. 2012. Condition-dependent transcriptome reveals high-level regulatory architecture in *Bacillus subtilis*. Science 335:1103–1106. https://doi.org/10.1126/science.1206848

23. Maaß S, Wachlin G, Bernhardt J, Eymann C, Fromion V, Riedel K, Becher D, Hecker M. 2014. Highly precise quantification of protein molecules per cell during stress and starvation responses in *Bacillus subtilis*. Mol Cell Proteomics 13:2260–2276. https://doi.org/10.1074/mcp.M113.035741

24. Maass S, Sievers S, Zühlke D, Kuzinski J, Sappa PK, Muntel J, Hessling B, Bernhardt J, Sietmann R, Völker U, Hecker M, Becher D. 2011. Efficient, global-scale quantification of absolute protein amounts by integration of targeted mass spectrometry and two-dimensional gel-based proteomics. Anal Chem 83:2677–2684. https://doi.org/10.1021/ac1031836

25. Weiss AKH, Loeffler JR, Liedl KR, Gstach H, Jansen-Dürr P. 2018. The fumarylacetoacetate hydrolase (FAH) superfamily of enzymes: multifunctional enzymes from microbes to mitochondria. Biochem Soc Trans 46:295–309. https://doi.org/10.1042/BST20170518

26. Timm DE, Mueller HA, Bhanumoorthy P, Harp JM, Bunick GJ. 1999. Crystal structure and mechanism of a carbon-carbon bond hydrolase. Structure 7:1023–1033. https://doi.org/10.1016/s0969-2126(99)80170-1

27. Ran T, Gao Y, Marsh M, Zhu W, Wang M, Mao X, Xu L, Xu D, Wang W. 2013. Crystal structures of Cg1458 reveal a catalytic lid domain and a common catalytic mechanism for the FAH family. Biochem J 449:51–60. https://doi.org/10.1042/BJ20120913

28. Hong H, Seo H, Park W, Kim K-J. 2020. Sequence, structure and function-based classification of the broadly conserved FAH superfamily reveals two distinct fumarylpyruvate hydrolase subfamilies. Environ Microbiol 22:270–285. https://doi.org/10.1111/1462-2920.14844

29. Guo T, Herman JK. 2023. Magnesium modulates *Bacillus subtilis* cell division frequency. J Bacteriol 205:e0037522. https://doi.org/10.1128/jb.00375-22

30. Carballido-López R, Errington J. 2003. The bacterial cytoskeleton: *in vivo* dynamics of the actin-like protein Mbl of *Bacillus subtilis*. Dev Cell 4:19–28. https://doi.org/10.1016/s1534-5807(02)00403-3

31. Garner EC, Bernard R, Wang W, Zhuang X, Rudner DZ, Mitchison T. 2011. Coupled, circumferential motions of the cell wall synthesis machinery and MreB filaments in *B. subtilis*. Science 333:222–225. https://doi.org/10.1126/science.1203285

32. Domínguez-Escobar J, Chastanet A, Crevenna AH, Fromion V, Wedlich-Söldner R, Carballido-López R. 2011. Processive movement of MreB-associated cell wall biosynthetic complexes in bacteria. Science 333:225–228. https://doi.org/10.1126/science.1203466

33. Park J, Cleary MB, Li D, Mattocks JA, Xu J, Wang H, Mukhopadhyay S, Gale EM, Cotruvo Jr JA. 2022. A genetically encoded fluorescent sensor for manganese(II), engineered from lanmodulin. Proc Natl Acad Sci U S A 119:e2212723119. https://doi.org/10.1073/pnas.2212723119

34. McCluskey K, Boudreault J, St-Pierre P, Perez-Gonzalez C, Chauvier A, Rizzi A, Beauregard PB, Lafontaine DA, Penedo JC. 2019. Unprecedented tunability of riboswitch structure and regulatory function by sub-millimolar variations in physiological Mg2. Nucleic Acids Res 47:6478–6487. https://doi.org/10.1093/nar/gkz316

35. Pircher H, von Grafenstein S, Diener T, Metzger C, Albertini E, Taferner A, Unterluggauer H, Kramer C, Liedl KR, Jansen-Dürr P. 2015. Identification of FAH domain-containing protein 1 (FAHD1) as oxaloacetate decarboxylase. J Biol Chem 290:6755–6762. https://doi.org/10.1074/jbc.M114.609305

36. Kelley LA, Mezulis S, Yates CM, Wass MN, Sternberg MJE. 2015. The Phyre2 web portal for protein modeling, prediction and analysis. Nat Protoc 10:845–858. https://doi.org/10.1038/nprot.2015.053

37. Gibrat JF, Madej T, Bryant SH. 1996. Surprising similarities in structure comparison. Curr Opin Struct Biol 6:377–385. https://doi.org/10.1016/s0959-440x(96)80058-3

38. Kubala G, Martell AE. 1981. Nuclear magnetic resonance investigation of the spontaneous decarboxylation of 2-oxalopropionic acid. 2. Species in solution. J Am Chem Soc 103:7609–7615. https://doi.org/10.1021/ja00415a032

39. Tsai CS. 1967. Spontaneous decarboxylation of oxalacetic acid. Can J Chem 45:873–880. https://doi.org/10.1139/v67-145

40. Park JO, Rubin SA, Xu Y-F, Amador-Noguez D, Fan J, Shlomi T, Rabinowitz JD. 2016. Metabolite concentrations, fluxes and free energies imply efficient enzyme usage. Nat Chem Biol 12:482–489. https://doi.org/10.1038/nchembio.2077

41. Koendjbiharie JG, van Kranenburg R, Kengen SWM. 2021. The PEP-pyruvate-oxaloacetate node: variation at the heart of metabolism. FEMS Microbiol Rev 45:fuaa061. https://doi.org/10.1093/femsre/fuaa061

42. Sauer U, Eikmanns BJ. 2005. The PEP-pyruvate-oxaloacetate node as the switch point for carbon flux distribution in bacteria. FEMS Microbiol Rev 29:765–794. https://doi.org/10.1016/j.femsre.2004.11.002

43. Das NB. 1937. Studies on the inhibition of the succinic and lactic-malic dehydrogenases. Biochem J 31:1124–1130. https://doi.org/10.1042/bj0311124

44. Wojtczak L, Wojtczak AB, Ernster L. 1969. The inhibition of succinate dehydrogenase by oxaloacetate. Biochim Biophys Acta (BBA) - Enzymol 191:10–21. https://doi.org/10.1016/0005-2744(69)90310-6

45. Zeyelmaker WP, Slater EC. 1967. The inhibition of succinate dehydrogenase by oxaloacetate. Biochim Biophys Acta 132:210–212. https://doi.org/10.1016/0005-2744(67)90214-8

46. Zeylemaker WP, Klaasse ADM, Slater EC. 1969. Studies on succinate dehydrogenase. V. Inhibition by oxaloacetate. Biochim Biophys Acta (BBA) - Enzymol 191:229–238. https://doi.org/10.1016/0005-2744(69)90242-3

47. PardeeAB, PotterVR. 1948. Inhibition of succinic dehydrogenase by oxalacetate. J Biol Chem 176:1085–1094.

48. Armstrong C, Staples JF. 2010. The role of succinate dehydrogenase and oxaloacetate in metabolic suppression during hibernation and arousal. J Comp Physiol B 180:775–783. https://doi.org/10.1007/s00360-010-0444-3

49. Fedotcheva NJ, Sharyshev AA, Mironova GD, Kondrashova MN. 1985. Inhibition of succinate oxidation and K+ transport in mitochondria during hibernation. Comp Biochem Physiol B 82:191–195. https://doi.org/10.1016/0305-0491(85)90151-8

50. Mookerjee SA, Gerencser AA, Watson MA, Brand MD. 2021. Controlled power: how biology manages succinate-driven energy release. Biochem Soc Trans 49:2929–2939. https://doi.org/10.1042/BST20211032

51. Petit M, Koziel R, Etemad S, Pircher H, Jansen-Dürr P. 2017. Depletion of oxaloacetate decarboxylase FAHD1 inhibits mitochondrial electron transport and induces cellular senescence in human endothelial cells. Exp Gerontol 92:7–12. https://doi.org/10.1016/j.exger.2017.03.004

52. Tam LT, Eymann C, Antelmann H, Albrecht D, Hecker M. 2007. Global gene expression profiling of Bacillus subtilis in response to ammonium and tryptophan starvation as revealed by transcriptome and proteome analysis. J Mol Microbiol Biotechnol 12:121–130. https://doi.org/10.1159/000096467

53. Wolff S, Antelmann H, Albrecht D, Becher D, Bernhardt J, Bron S, Büttner K, van Dijl JM, Eymann C, Otto A, Tam LT, Hecker M. 2007. Towards the entire proteome of the model bacterium Bacillus subtilis by gel-based and gel-free approaches. J Chromatogr B Analyt Technol Biomed Life Sci 849:129–140. https://doi.org/10.1016/j.jchromb.2006.09.029

54. Meyer FM, Gerwig J, Hammer E, Herzberg C, Commichau FM, Völker U, Stülke J. 2011. Physical interactions between tricarboxylic acid cycle enzymes in Bacillus subtilis: evidence for a metabolon. Metab Eng 13:18–27. https://doi.org/10.1016/j.ymben.2010.10.001

55. Beaufay F, Coppine J, Mayard A, Laloux G, De Bolle X, Hallez R. 2015. A NAD-dependent glutamate dehydrogenase coordinates metabolism with cell division in Caulobacter crescentus. EMBO J 34:1786–1800. https://doi.org/10.15252/embj.201490730

56. Sperber AM, Herman JK. 2017. Metabolism shapes the cell. J Bacteriol 199:e00039-17. https://doi.org/10.1128/JB.00039-17

57. Hill NS, Buske PJ, Shi Y, Levin PA. 2013. A moonlighting enzyme links Escherichia coli cell size with central metabolism. PLoS Genet 9:e1003663. https://doi.org/10.1371/journal.pgen.1003663

58. Weart RB, Lee AH, Chien A-C, Haeusser DP, Hill NS, Levin PA. 2007. A metabolic sensor governing cell size in bacteria. Cell 130:335–347. https://doi.org/10.1016/j.cell.2007.05.043

59. Sterlini JM, Mandelstam J. 1969. Commitment to sporulation in Bacillus subtilis and its relationship to development of actinomycin resistance. Biochem J 113:29–37. https://doi.org/10.1042/bj1130029

60. Karimova G, Pidoux J, Ullmann A, Ladant D. 1998. A bacterial two-hybrid system based on a reconstituted signal transduction pathway. Proc Natl Acad Sci U S A 95:5752–5756. https://doi.org/10.1073/pnas.95.10.5752

61. Harwood CR, Cutting SM. 1990. Molecular biological methods for Bacillus. Wiley, Chichester, New York.

62. Rasband WS. 1997. ImageJ. U. S. National Institutes of Health, Bethesda, Maryland, USA. Available from: https://imagej.nih.gov/ij

63. Kabsch W. 2010. Xds. Acta Crystallogr D Biol Crystallogr 66:125–132. https://doi.org/10.1107/S0907444909047337

64. Evans P. 2006. Scaling and assessment of data quality. Acta Crystallogr D Biol Crystallogr 62:72–82. https://doi.org/10.1107/S0907444905036693

65. Evans PR, Murshudov GN. 2013. How good are my data and what is the resolution? Acta Crystallogr D Biol Crystallogr 69:1204–1214. https://doi.org/10.1107/S0907444913000061

66. Vagin A, Teplyakov A. 2010. Molecular replacement with MOLREP. Acta Crystallogr D Biol Crystallogr 66:22–25. https://doi.org/10.1107/S0907444909042589

67. Emsley P, Cowtan K. 2004. Coot: model-building tools for molecular graphics. Acta Crystallogr D Biol Crystallogr 60:2126–2132. https://doi.org/10.1107/S0907444904019158

68. Liebschner D, Afonine PV, Baker ML, Bunkóczi G, Chen VB, Croll TI, Hintze B, Hung LW, Jain S, McCoy AJ, Moriarty NW, Oeffner RD, Poon BK, Prisant MG, Read RJ, Richardson JS, Richardson DC, Sammito MD, Sobolev OV, Stockwell DH, Terwilliger TC, Urzhumtsev AG, Videau LL, Williams CJ, Adams PD. 2019. Macromolecular structure determination using X-rays, neutrons and electrons: recent developments in Phenix. Acta Crystallogr D Struct Biol 75:861–877. https://doi.org/10.1107/S2059798319011471

69. Moriarty NW, Grosse-Kunstleve RW, Adams PD. 2009. electronic ligand builder and optimization workbench (eLBOW): a tool for ligand coordinate and restraint generation. Acta Crystallogr D Biol Crystallogr 65:1074–1080. https://doi.org/10.1107/S0907444909029436

70. Niesen FH, Berglund H, Vedadi M. 2007. The use of differential scanning fluorimetry to detect ligand interactions that promote protein stability. Nat Protoc 2:2212–2221. https://doi.org/10.1038/nprot.2007.321

Supplementary materials

***Bacillus subtilis* YisK possesses oxaloacetate decarboxylase activity and exhibits Mbl-dependent localization**

Tingfeng Guo[1], Anthony M. Sperber[1], Inna V. Krieger[1], Yi Duan[1], Veronica Chemelewski[1], James C. Sacchettini[1,2], and Jennifer K. Herman[1]*

Short title: YisK decarboxylates oxaloacetate

[1]Department of Chemistry, Texas A&M University, College Station, TX

[2]Department of Chemistry, Texas A&M University, College Station TX

Corresponding author*
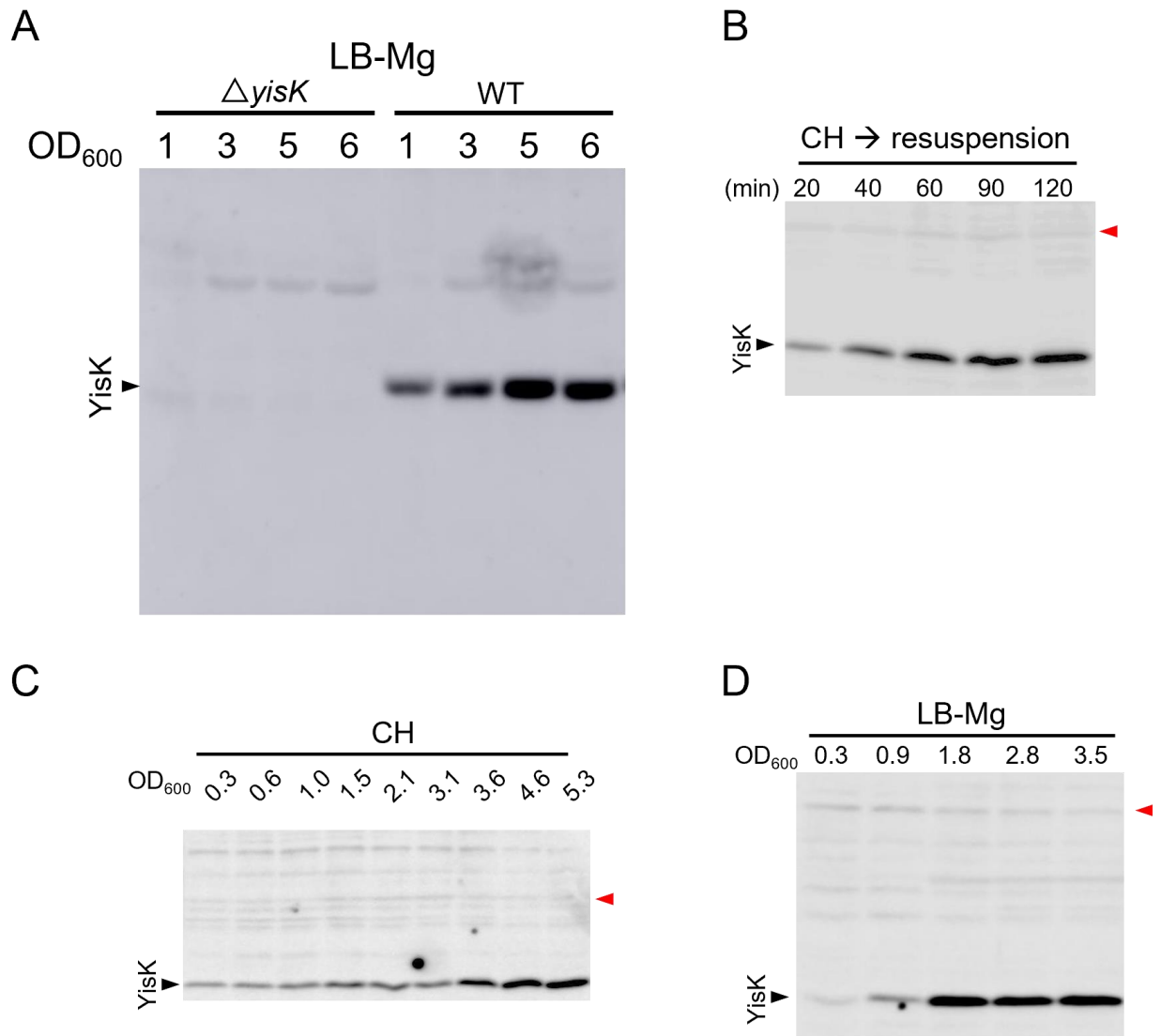
Figure S1. (A) Specificity of α-YisK rabbit polyclonal antibody (serum). Wild-type (BJH004) and Δ*yisK* (BYD278) were grown at 37°C in LB-Mg and collected at the indicated OD_{600}. (B-C) Westerns blots from Figure 1. The red triangles indicate cross-reacting background signal that serves as a loading control.
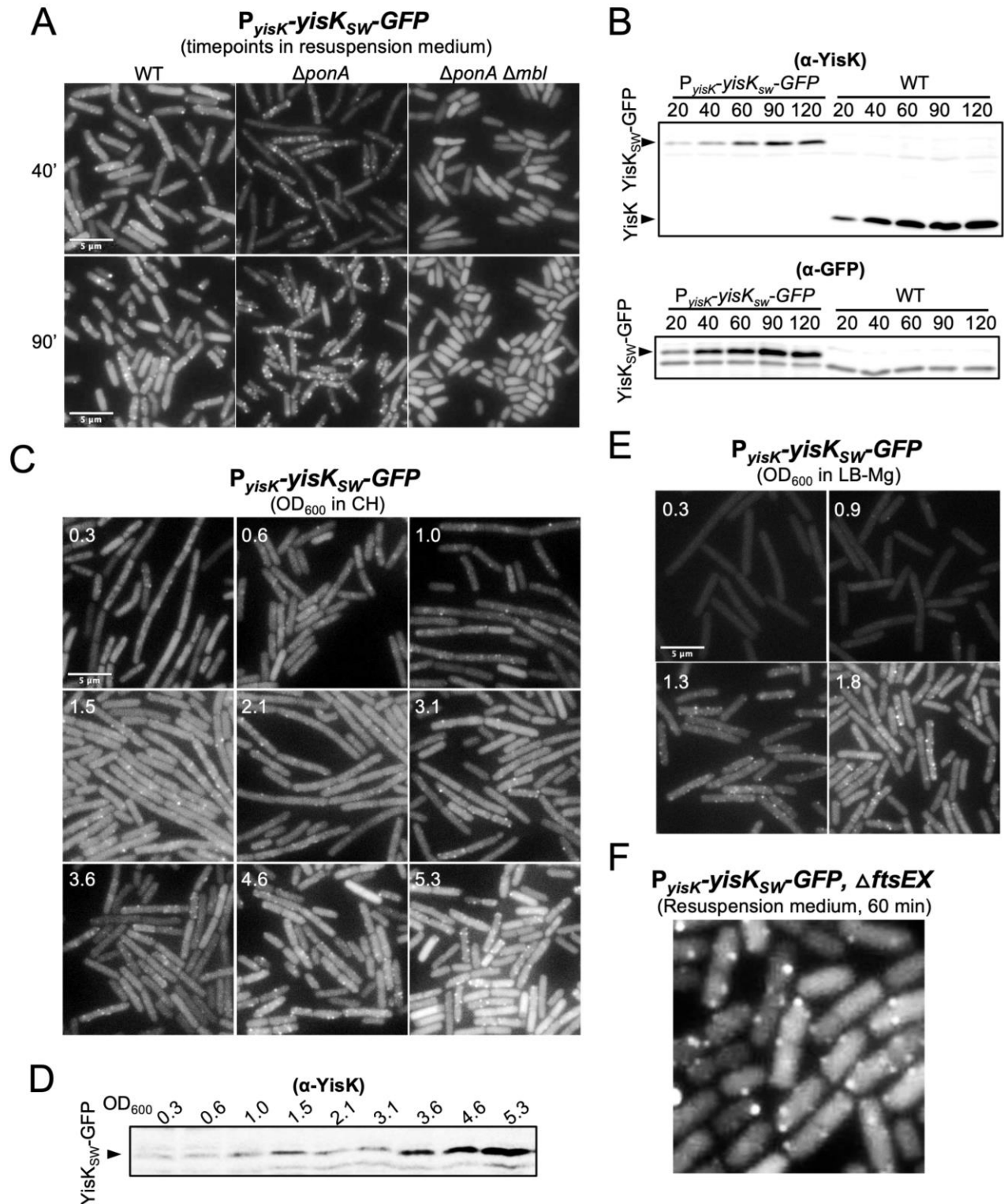
Figure S2. (A, C, E, and F) Representative micrographs of cells harboring P_{yisK}-$yisK_{SW}$-GFP during growth in the indicated media. Images within the same medium are shown at the same magnification and scaled identically in the GFP channel. Western blot analysis in (B) sporulation by resuspension medium and (D) CH.

A

```
YisK    MKFATGELYNRMFVGLIIDDEKIMDLQKAEKKLFELETIPGSLIECIAEGDKFVAHARQL    60
FAHD1   ------------------------------------------------------------     0
Cg1458  -----------------------------MRFGRIATPDGMCFCSIEGEGDDVANLTA     29


                                                    Lid region
                                                   ‾‾‾‾‾‾‾‾‾‾‾
YisK    AEWAKK--PNDELGSFMYSLSEVKLHAPIPKPSKNIICIGKNYRDHAIEMGSEADIPEHP    118
FAHD1   -----------MG----IMAASRPLSRFWEWGKNIVCVGRNYADHVREMRSAV--LSEP     42
Cg1458  REIEGTPFTEPKFTGREWPLKDVRLLAPM--LPSKVVAIGRNYADHVAEVFKKSAESLPP     87
                  :       :   : :     .::..*:** **. *:  .        *

YisK    MVFTKSPVTVTGHGDIVKSHEEVTSQLDYEGELAVVIGKSGTRISKEDAYDHVFGYTIVN    178
FAHD1   VLFLKPSTAYAPEGSPI-LMPAYTRNLHHELELGVVMGKRCRAVPEAAAMDYVGGYALCL    101
Cg1458  TLFLKPPTAVTGPESPI-RIPSFATKVEFEGELAVVIGKPCKNVKADDWKSVVLGFTIIN    146
          :* * .: : . :         : ::..* **.**:**     :       . * *:::

              FAHD1 insertion
             ‾‾‾‾‾‾‾‾‾‾‾‾‾
YisK    DITARDLQKRHK----QFFIGKSLDTTCPMGPVLVHKSSIQEPERLK----VETRVNGEL    230
FAHD1   DMTARDVQDECKKKGLPWTLAKSFTASCPVSAF-VPKEKIPDPHKLK----LWLKVNGEL    156
Cg1458  DVSSRDLQFADG----QWARAKGIDTFGPIGPWIETDINSIDLDNLPIKARLTHDGETQL    202
        *::::**:*       :   .*.: :  *:.    .. . : ..*   :      : :*

                                        YisK insertion
                          ‾‾‾‾‾‾‾‾‾‾‾‾  ‾‾‾‾‾‾‾‾‾‾‾
YisK    RQSGSASDMIFSIPELIETLSKGMTLEAGDIIATGTPSGVGKGFTPPKFLRSGDKIDITI    290
FAHD1   RQEGETSSMIFSIPYIISYVSKIITLEEGDIILTGTPKGVGPVKEN-------DEIEAGI    209
Cg1458  KQDSNSNQMIMKMGEIIEFITASMTLLPGDVIATGSPAGTEAMV-------DGDYIEIEI    255
        :*...:..**:.:  :*. ::  :**  **:* **:* *.         * *:   *

YisK    DPIGTLSNQIG----    301
FAHD1   HGLVSMTFKVEKPEY    224
Cg1458  PGIGKLGNPVVDA--    268
          : .:    :
```
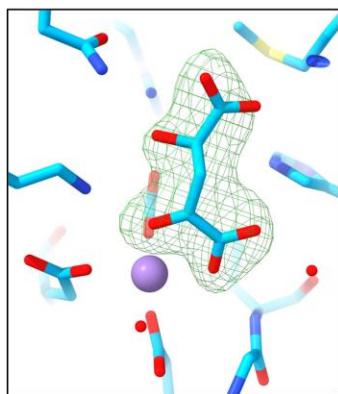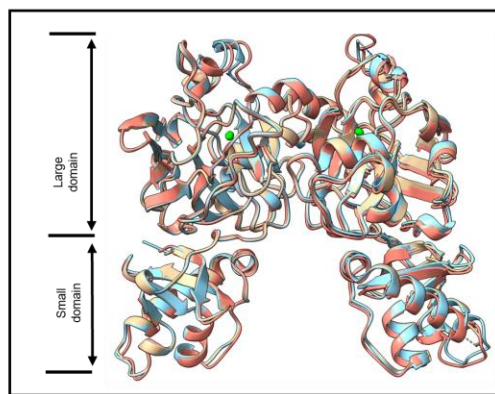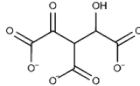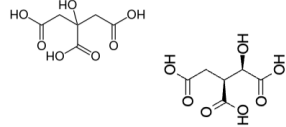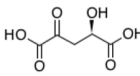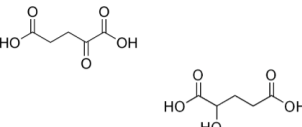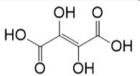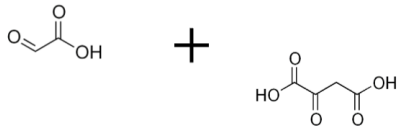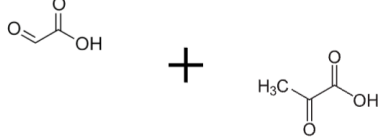
B

C

Figure S3. (A) Clustal O sequence alignment of YisK, FAHD1, and Cg1458. Residues corresponding to the small domain of YisK are highlighted in yellow with the E30 residue in red. Catalytic histidine (blue). Residues coordinating Mn^{2+} (pink). Invariant residues of active site (green). Residues that vary in/around the active site between YisK and FAHD1 and/or Cg1458 (grey). (B) Product of oxalomalate decarboxylation, HOGA, bound in the active site of YisK. Polder omit map contoured at 5 sigma le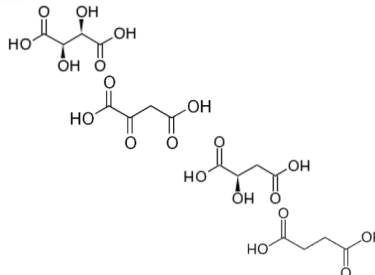vel displayed as green mesh. Model is shown as sticks with protein and ligand carbons (light blue), oxygens (red), nitrogens (blue) and Mn2+ (purple). (C) Overlay of YisK structures in unliganded (8SUU, beige), oxalate-bound (8SKY, salmon), and HOGA-bound (8SUT, light blue). The Mn^{2+} ion is shown as a green sphere.

1.0 mM compound	ΔTm °C	structure
oxalomalate	**16**	
citrate	ns	
isocitrate	ns	
D-4-hydroxy-2-oxoglutarate	**16.5**	
α-Ketoglutaric acid	ns	
hydroxyglutarate	ns	
dihydroxyfumurate	**9**	
L-tartrate	**9**	
oxaloacetate	ns	
L-malate	ns	
succinate	ns	
oxalate	**17**	
glyoxylate + oxaloacetate	**17**	
glyoxylate	ns	
oxaloacetate	ns	
glyoxylate + pyruvate	**4**	
glyoxylate	ns	
pyruvate	ns	

Figure S4. YisK differential scanning fluorimetry screen. Assay contained 1.0 µM YisK, 1.0 mM MnCl$_2$, 1.0 mM MgCl$_2$, 1.0 mM CaCl$_2$ and 1.0 mM of each the indicated compounds. Compounds in bold stabilized YisK significantly (>2.5°C). Compounds that stabilized YisK ≤ 2.5°C were not considered significant (ns). Oxaloacetate spontaneously decarboxylates to pyruvate and CO$_2$ and may be unstable in the assay.
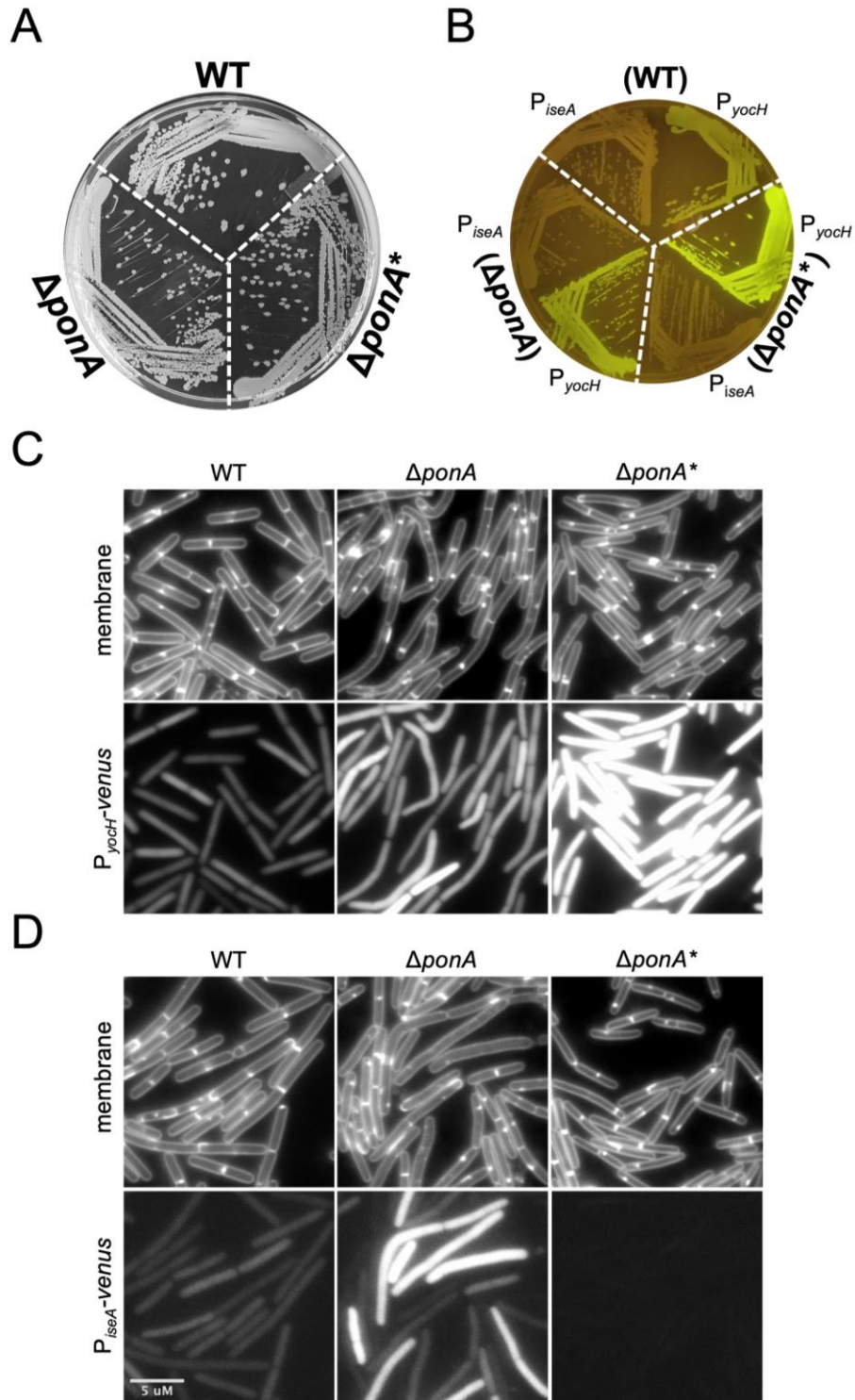
Figure S5. (A) Growth of WT 168 (BJH004), Δ*ponA* (BTG042), and Δ*ponA** (*walH* Q242stop) on an LB-Mg plate. Strains harboring P*yocH*-*venus* or P*iseA*-*venus* were grown at at 37°C (B) on an LB-Mg plate and imaged under blue light or (C and D) imaged during exponential stage growth in liquid LB-Mg. Membranes were stained with TMA. All images are shown at the same magnification. The images for each reporter set are scaled identically (1000-16,500 for P*yocH*-*venus* and 200-1000 for P*iseA*-*venus*).

WT YisK, T_m = 55.5 °C			
1.0 mM each compound	ΔT_m °C	1.0 mM each compound	ΔT_m °C
acetate*	ns	NAD+	ns
ammonium chloride	ns	NADH	ns
formate	ns	NADP+	ns
urea*	ns	ATP	ns
D-glyceric acid*	ns	ADP	ns
D-3-phosphoglycerate	ns	AMPPNP	ns
phosphoenolpyruvate	ns	D-malate	ns
pyruvate*	ns	D-malate + fumarate	ns
pyruvate + urea*	ns	fumarate + pyruvate	ns
citrate*	ns	L-malate*	ns
isocitrate*	ns	L-lactate*	ns
2-oxoglutarate*	ns	glycolic acid	ns
succinic semialdehyde*	ns	dihydroxyfumurate	9.0
succinate*	ns	**oxalomalate****	**16.0**
fumarate*	ns	**D-4-hydroxy-2-oxoglutarate***	**16.5**
oxaloacetate**	ns	glyoxylate*	ns
oxaloacetate** + acetate	ns	glyoxylate + fumarate *	3.5
oxaloacetate** + pyruvate	ns	glyoxylate + malate*	3.5
oxaloacetate** + urea	ns	glyoxylate + pyruvate*	4.0
glyoxylate + succinate*	ns	**glyoxylate + oxaloacetate****	**17.0**
glyoxylate + urea*	ns	L-tartrate*	9.0
glyoxylate + 2-oxoglutarate*	ns	L-tartrate + acetate*	7.5
D-alanine	ns	L-tartrate + urea*	7.5
L-asparagine	ns	**L-tartrate +glyoxylate***	**10.0**
L-aspartate	ns	**oxalate***	**17.0**
L-glutamate	ns	**oxalate + fumarate***	**16.5**
D-aspartate	ns	**oxalate + succinate***	**17.0**
D-glutamate	ns	**oxalate + pyruvate***	**17.5**
D-alanine-D-alanine	ns	**oxalate + malate***	**17.5**
cyclic D-alanine L-alanine	ns	**oxalate + L-tartrate***	**18.0**
meso-2,6-diaminopimelic acid (mDAP)	ns	**oxalate + oxaloacetate****	**18.5**
ampicillin	ns	**oxalate + 2-oxoglutarate***	**19.0**
carbenicillin	ns		
2-oxoadipic acid	ns		

Table S1. Compounds tested in thermal assay. Assays contained either 10.0 µM YisK, 5.0 mM MnCl$_2$, and 1.0 mM of each the indicated compounds or, when indicated by (*), 1.0 µM YisK, 1.0 mM MnCl$_2$, 1.0 mM MgCl$_2$, 1.0 mM CaCl$_2$ and 1.0 mM of each the indicated compounds. Compounds in bold stabilized YisK ≥ 10℃. Compounds that stabilized YisK ≤ 2.5ºC were not considered significant (ns). (**) compounds may be unstable in assay.

Table S2. Strains

Strain	Wildtype (WT) Strains	Reference
BJH004	*Bacillus subtilis* 168	Bacillus Genetic Stock Center 1A1
	***Bacillus subtilis* 168 derivatives**	
BKE22320	△*ponA*::*erm*	Bacillus Genetic Stock Center
BAS041	*amyE::P_hy-yisK (spec)*	(1)
BGD110	*amyE::P_iseA-optRBS-venus (cat)*	(2)
BGD300	*amyE::P_yocH-optRBS-venus (cat)*	(2)
BJH846	*yisK::yisK_SW-GFP E148A E150A (spec)*	Fig 6
BTG010	*amyE::P_hy-yisK E148A E150A (spec)* *yhdG::P_hy-yisK E148A E150A (phleo)*	Fig 6
BTG011	*amyE::P_hy-yisK E30A (spec)* *yhdG::P_hy-yisK E30A (phleo)*	Fig 6
BTG042	△*ponA::erm (clean background)*	Fig S5
BTG068	*amyE::P_hy-yisK_SW-GFP (spec)*	Fig 3
BTG078	*yisK::yisK_SW-GFP*	Fig 2, Fig S2
BTG081	*yisK::yisK_SW-GFP, ponA::erm*	Fig 3
BTG082	*yisK::yisK_SW-GFP, ponA::erm, △mbl (kan-linked)*	Fig 3
BTG088	*yisK::yisK_SW-GFP E30A*	Fig 6
BTG159	*amyE::P_hy-yisK_SW-GFP E148A E150A (spec), △yisK*	This study
BTG160	*amyE::P_hy-yisK_SW-GFP E148A E150A (spec)*	Fig 7
BTG169	*trpC+*	(3)
BTG278	*amyE ::P_yocH-optRBS-venus (cat)*	Fig S5
BTG279	*amyE::P_iseA-optRBS-venus (cat)*	Fig S5
BTG468	△*ponA*::*erm (walH Q242stop)* *amyE ::P_yocH-optRBS-venus (cat)*	Fig S5
BTG469	△*ponA*::*erm (walH Q242stop)* *amyE::P_iseA-optRBS-venus (cat)*	Fig S5
BTG470	△*ponA::erm (clean background)* *amyE ::P_yocH-optRBS-venus (cat)*	Fig S5
BTG471	△*ponA::erm (clean background)* *amyE::P_iseA-optRBS-venus (cat)*	Fig S5
BTG607	*amyE::P_hy-yisK E30A (spec), trpC+*	Fig 7D
BTG608	*amyE::P_hy-yisK (spec), trpC+*	Fig 7D
BYD074	*amyE::P_hy-yisK (spec)* *yhdG::P_hy-yisK (phleo)*	(1)
BYD172	*ponA*::*erm (walH Q242stop)*	BKE22320 (4)
BYD278	△*yisK*	(1)
BYD587	*amyE::P_hy -yisK E148A E150A (spec)*	Fig 6
BYD588	*amyE::P_hy -yisK E30A (spec)*	Fig 6
BTH101	*F-, cya-99, araD139, galE15, galK16, rpsL1 (Str r), hsdR2, mcrA1, mcrB1*	(5)
cYD784	*yisK-pET24b (kan)*	This study
cYD982	*YisK-T25 (kan), empty-T18 (amp)*	Fig 6
cYD984	*YisK-T18 (amp), empty-T25 (kan)*	Fig 6

cYD1077	*yisK-pET24b E148A E150A (kan)*	This study
cYD1080	*YisK-T18 (amp), YisK-T25 (kan)*	Fig 6
cYD1154	*yisK-pET24b E30A (kan)*	This study
cYD1157	*YisK-T18 E30A (amp), YisK-T25 E30A (kan)*	Fig 6
cYD1158	*empty-T18 (amp), YisK-T25 E30A (kan)*	Fig 6
cYD1159	*empty-T25 (kan), YisK-T18 E30A (amp)*	Fig 6

Table S3. Plasmids

Plasmid	Description	Reference
pDR111	*amyE::P$_{hy}$ (spec)(amp)*	David Rudner
pMiniMAD2	ori^{BsTs} *(amp)(erm)*	(6)
pJH051	*pMiniMAD2 yisK$_{SW}$-GFP E148A E150A (amp)(erm)*	This study
pTG004	*pMiniMAD2 yisK$_{SW}$-GFP (amp)(erm)*	This study
pTG006	*pMiniMAD2 yisK$_{SW}$-GFP E30A (amp)(erm)*	This study
pKT25	*T25-empty (kan)*	Tom Bernhardt
pKNT25	*empty-T25 (kan)*	Tom Bernhardt
pCH364	*empty-T18 (amp)*	Tom Bernhardt
pYD216	*YisK-T18 (amp)*	This study
pYD218	*YisK-T25 (kan)*	This study
pET24b	*C-terminal 6X-His tag vector (kan)*	Novagen
pYD104	*yisK-pET24b (kan)*	This study
pYD228	*yisK-pET24b E148A E150A (kan)*	This study
pYD229	*YisK-T25 E30A (kan)*	This study
pYD230	*YisK-T18 E30A (amp)*	This study
pYD231	*yisK-pET24b E30A (kan)*	This study

Plasmid inserts and fusions were confirmed by sequencing.

Table S4. Oligonucleotides

OLIGO	SEQUENCE 5' TO 3'
oAS253	TACCGTTCGTATAGCATACATTATACGAAGTTATGATTTTATGACCGATGATGAAGA
oAS254	TACCGTTCGTATAATGTATGCTATACGAAGTTATAACTCTCTCCCAAAGTTGATC
oAS334	TTATCTGAATTCTACCGGCTGGCTGATGGTTC
oAS335	AAGTTCCCCTGTCGCAAATTTCATGTTATTCCTCCATCATCTTTTAAA
oAS336	TTTAAAAGATGATGGAGGAATAACATGAAATTTGCGACAGGGGAAC
oAS337	GCGTAAGGATCCTCAGCCAATTTGGTTTGACAGC

oEA35	GGATAACAATTAAGCTTACATAAGGAGGAACTACTATGAAATTTGCGACAGGGGAACTT
oEA36	TTCCACCGAATTAGCTTGCATGCGGCTAGCCCAGTTTTATTCAGCCAATTTGGT
oJH159	CTGCAGGAATTCGACTCTCTA
oJH346A	GCATGGATGAACTATACAAAGG
oJH347	GTAAAACGACGGCCAGTGAATTCTACCGGCTGGCTGATGGTTC
oJH348	CTGCAGGTCGACTCTAGAGGATCCTCAGCCAATTTGGTTTGACAGC
oJH349	GGATCCTCTAGAGTCGACCTGCAGGC
oJH350	GAATTCACTGGCCGTCGTTTTACAAC
oTG001	GGTTCTGGGTCAATGAGTAAAGGAGAAGAAC
oTG002	TGATCCACTGCCTTTGTATAGTTCATCCATG
oTG009	TACAAAGGCAGTGGATCAGCTGATATTCCGGAGCATCCGATG
oTG010	ACTCATTGACCCAGAACCCTCGCTCCCCATTTCAATCGCGTG
oTG109	AATCCCAATCGCCCCAAAGGCTCCGGAGGCAG
oTG110	CATAGTAGTTCCTCCTTATGTAAGCTTAATTG
oTG215	GCTAGCCGCATGCAAGCTAAT
oTG216	CTGCTTCATTTTCTCATCTCTTCAG
oYD262	GCATGGATCC GTAACACACAGGAAACAGCTATGTTTGCAAGGGATATTGGTA
oYD263	GCATGAATTCGAACCGCTACCGCTTAGTTTGCGTTTAGGAAG
oYD298	GCATGGATCCGTAACACACAGGAAACAGCTATGAAATTTGCGACAGGGGAAC
oYD299	GCATGAATTCGAACCGCTACCGCCAATTTGGTTTGACAGCGTT
oYD309	AGATAAGCTAGCTTAGCCAATTTGGTTTGACAGCG
oYD479	GCATGGATCCGTAACACACAGGAAACAGCTATGATTAAAATTCTCGGGCGC
oYD480	GCATGAATTCGAACCGCTACCTACTCGCAGAAACTTGCGGA
oYD545	TACCTCTCAGCTTGATTATGCGGGAGCACTTGCTGTCGTGATCGGAA
oYD546	TTCCGATCACGACAGCAAGTGCTCCCGCATAATCAAGCTGAGAGGTA
oYD577	TATGGATTTGCAGAAGGCTGCAAAAAAACTGTTTGAACTTG
oYD578	CAAGTTCAAACAGTTTTTTTGCAGCCTTCTGCAAATCCATA

Text S1. Strain construction

Deletion/knockout strains were confirmed by PCR. Point mutations were confirmed by PCR and sequencing.

BJH846 [*yisK::yisK$_{SW}$-GFP E148A E150A*] was created by transforming *B. subtilis* 168 with plasmid pJH051 and following the alleic replacement process.

BTG010 [*amyE::P$_{hy}$ -yisK E148A E150A (spec), yhdG::P$_{hy}$-yisK E148A E150A (phleo)*] was created by transforming *B. subtilis 168* with a linear Gibson assembly product encoding three fragments including a region upstream of *amyE* with a spectinomycin cassette using oTG109 and oTG110, the *P$_{hy}$-yisK E148A E150A* using oEA35 and oEA36 amplified from pYD228, a region downstream of *amyE* into *B. subtilis* 168 using oTG215 and oTG216, and selecting for growth on LB plates containing 100 µg ml-1 spectinomycin. The confirmed clone was then transformed ScaI-linearized plasmid *yhdG::P$_{hy}$-yisK E148A E150A (phleo),* selecting for for growth on LB plates containing 400 µg ml-1 phleomycin.

BTG011 [*amyE::P$_{hy}$ -yisK E30A (spec), yhdG::P$_{hy}$-yisK E30A (phleo)*] *amyE::P$_{hy}$ -yisK E30A (spec)* was created by transforming *B. subtilis* 168 with a linear Gibson assembly product encoding three fragments including a region upstream of *amyE* with a spectinomycin cassette using oTG109 and oTG110, the *P$_{hy}$-yisK E30A* using oEA35 and oEA36 amplified from pYD231, a region downstream of *amyE* into *B. subtilis* 168 using oTG215 and oTG216, and selecting for for growth on LB plates containing 100 µg ml-1 spectinomycin. The confirmed clone was then transformed with ScaI-linearized plasmid *yhdG::P$_{hy}$-yisK E30A (phleo),* selecting for for growth on LB plates containing 400 µg ml-1 phleomycin.

BTG042 [△*ponA::erm*] was created by transforming BJH004 with genomic DNA from BYD172 [△*ponA::erm*] selecting for growth on LB plates containing 1 µg/ml erythromycin (erm) plus 25 µg/ml lincomycin (MLS) and 10.0 mM MgCl$_2$.

   In the process of generating the strains for the experiments in Fig 2, we noted that the Δ*ponA*::*erm* strain we made (designated as Δ*ponA*) grew slightly slower than the strain obtained from the *Bacillus* Genetic Stock Center (designated as Δ*ponA**)(Fig S5A). In addition, we noted that even when grown in the presence of excess MgCl$_2$, the slower growing Δ*ponA* cells were more irregular in shape than the Δ*ponA** cells (Fig S5C). Whole genome sequencing revealed Δ*ponA** possessed a mutation in *walH* (CAG→TAG; Q242stop), a gene encoding a negative regulator of the WalRK envelope stress response (7, 8). Consistent with loss of *walH* function, Δ*ponA** cells exhibited strong activation of a WalR-activated promoter (P$_{yocH}$) and enhanced repression of a WalR-repressed promoter (P$_{iseA}$) compared to a wildtype control (Fig S5B and S5C). In contrast, the slower growing Δ*ponA* strain used in the YisK experiments exhibited only modest and heterogeneous activation of P$_{yocH}$ (Fig S5B and S5C) and repression of P$_{iseA}$ (Fig S5D) relative to wildtype. These results suggest that in the absence of *ponA*, a constitutively active WalRK response is favorable to growth.

BTG068 [*amyE::P$_{hy}$-opt rbs-yisK$_{SW}$-GFP (spec) (E111-GFP-A112)*] was created by transforming *B. subtilis* 168 with a linear Gibson assembly product encoding three fragments including a region upstream of *amyE* with a spectinomycin cassette using oTG109 and oTG110, the *P$_{hy}$-opt rbs-yisK$_{SW}$-GFP (spec) E111-GFP-A112* using oEA35 and oTG10, oEA36 and oTG009, oTG001 and oTG002, a region downstream of *amyE* into *B. subtilis* 168 using oTG215 and oTG216, and selecting for for growth on LB plates containing 100 µg ml-1 spectinomycin. The detailed protocol is mentioned in the lab previous work (1).

Allelic replacement of wild-type *yisK* with *yisK-GFP*

The native *yisK_SW-GFP* were generated through allelic replacement. Briefly, *yisK_SW-GFP* gene was generated using overlap extension PCR and cloned into the vector pMiniMad2. The plasmid was then purified from TG-1 E. coli and used to transform *B. subtilis* 168. Single-crossover integration was selected for by plating cells at 37°C in the presence of erythromycin (1 µg/ml) and lincomycin (25 µg/ml). Six independent colonies were inoculated into six independent 3 ml LB cultures and grown overnight at room temperature in a rotary drum set at 60 rpm. The cultures were back-diluted 150X in fresh LB, and grown 8 hr at room temperature. 100 µl of a 10^{-5} dilution of each culture was plated on 6 independent LB plates and incubated overnight at 37°C. Ten single colonies from each plate were patched on an LB plate and an LB plate supplemented with erythromycin (1 µg/ml) and lincomycin (25 µg/ml). After streaking for isolated colonies, genomic DNA was collected from several antibiotic sensitive colonies obtained from independent cultures. The YisK region was then PCR-amplified and strains carrying the desired mutation were identified by sequencing with primers oAS334 and oAS337.

BTG078 [*yisK::yisK_SW-GFP*] was created by transforming *B. subtilis* 168 with a plamid pTG004 and following the alleic replacement process.

BTG081 [*yisK::yisK_SW-GFP, △pona::erm*] was created by transforming BTG78 with genomic DNA from BYD172 [*△ponA::erm*] selecting for growth on LB plates containing 1 µg/ml erythromycin (erm) plus 25 µg/ml lincomycin (MLS) and 10.0 mM $MgCl_2$.

BTG082 [*yisK::yisK_SW-GFP, △ponA::erm, △mbl (kan linked)*] was created by transforming BTG81 with genomic DNA from BYD258 [*△mbl (Kan linked)*](9) and selecting for growth on LB plates containing 10 µg/ml kanamycin and 10mM $MgCl_2$.

BTG088 [*yisK::yisK_SW-GFP E30A*] was created by transforming *B. subtilis* 168 with a plamid pTG006 and following the alleic replacement process.

BTG160 [*amyE::P_hy-yisK_SW-GFP E148A E150A (spec)*] was created by transforming *B. subtilis* 168 with a linear gibson assembly product encoding three fragments including a region upstream of *amyE* with a spectinomycin cassette using oTG109 and oTG110, the *P_hy-opt rbs-yisK (spec) E111-GFP-A112 E148A E150A* using oEA35 and oTG10, oEA36 and oTG009, oTG001 and oTG002, a region downstream of *amyE* into *B. subtilis* 168 using oTG215 and oTG216, and selecting for for growth on LB plates containing 100 µg ml-1 spectinomycin.

BTG278 [*amyE ::P_yocH-optRBS-venus (cat)*] was created by transforming BJH004 with genomic DNA from bGD300. *amyE ::P_yocH-optRBS-venus (cat)* was selected for by growth on LB plates containing 5 µg/ml chloramphenicol (cat).

BTG279 [*amyE ::P_iseA-optRBS-venus (cat)*] was created by transforming BJH004 with genomic DNA from BGD110 [*amyE ::P_iseA-optRBS-venus (cat)*] and selecting for growth on LB plates containing 5 µg/ml chloramphenicol (cat).

BTG468 [*△ponA::erm (suppressor), amyE ::P_yocH-optRBS-venus (cat)*] was created by transforming BYD172 with genomic DNA from bGD300. *amyE ::P_yocH-optRBS-venus (cat)*] was selected for by growth on LB plates containing 5 µg/ml chloramphenicol (cat).

BTG469 [*△ponA*::erm (suppressor), amyE ::P_iseA-optRBS-venus (cat)*] was created by transforming BYD172 with genomic DNA from bGD110. *amyE ::P_iseA-optRBS-venus (cat)*] was selected for by growth on LB plates containing 5 µg/ml chloramphenicol (cat).

BTG470 [△*ponA*::erm*, *amyE ::P$_{yocH}$-optRBS-venus (cat)*] was created by transforming BTG42 with genomic DNA from bGD300. *amyE ::P$_{yocH}$-optRBS-venus (cat)* was selected for by growth on LB plates containing 5 µg/ml chloramphenicol (cat).

BTG471 [△*ponA::erm, amyE ::P$_{iseA}$-optRBS-venus (cat)*] was created by transforming BTG042 with genomic DNA from bGD110. *amyE ::P$_{iseA}$-optRBS-venus (cat)* was selected for by growth on LB plates containing 5 µg/ml chloramphenicol (cat).

BTG607 [*amyE::P$_{hy}$ -yisK E30A (spec), tryptophan protrophic*] was created by transforming BTG169 tryptophan protrophic strian with genomic DNA from *amyE::P$_{hy}$ -yisK E30A (spec)* [*amyE::P$_{hy}$ -yisK E30A (spec)*] selecting for growth on LB plates containing 100 µg ml-1 spectinomycin.

BTG608 [*amyE::P$_{hy}$ -yisK (spec), tryptophan protrophic*] was created by transforming BTG169 tryptophan protrophic strian with genomic DNA from BAS41 [*amyE::P$_{hy}$ -yisK (spec)*] selecting for growth on LB plates containing 100 µg ml-1 spectinomycin.

BYD587 [*amyE::P$_{hy}$ -yisK (spec)*] was created by transforming *B. subtilis* 168 with a linear Gibson assembly product encoding three fragments including a region upstream of *amyE* with a spectinomycin cassette using oTG109 and oTG110, the *P$_{hy}$-yisK WT* using oEA35 and oEA36 amplified from qYD104, a region downstream of *amyE* into *B. subtilis* 168 using oTG215 and oTG216 and selecting for for growth on LB plates containing 100 µg ml-1 spectinomycin. The detailed protocol is described in previous work (1).

BYD588 [*amyE::P$_{hy}$ -yisK E30A (spec)*] was created by transforming *B. subtilis* 168 with a linear Gibson assembly product encoding three fragments including a region upstream of *amyE* with a spectinomycin cassette using oTG109 and oTG110, the *P$_{hy}$-yisK E30A* using oEA35 and oEA36 amplified from qYD497, a region downstream of *amyE* into *B. subtilis* 168 using oTG215 and oTG216 and selecting for for growth on LB plates containing 100 µg ml-1 spectinomycin. The detailed protocol is described in previous work (1).

Plasmid construction

pJH051 was generated with overlap extension PCR and Gibson assembly. The "UP" product was amplified from *B. subtilis 168* genomic DNA with primer pair oAS334/oAS335. The "DOWN" product was amplified from BTG059 with primer pair oAS336/oAS337. The two PCR products were used as template for overlap extension PCR with primer pair oAS334/oAS337. The PCR product was then amplified with oJH347 and oJH348 to create the insert. pMiniMAD2 was amplified with oJH049 and oJH050 to create a linear vector. The insert and vector were enzymatically assembly using the method and transformed into DH5alpha selecting for ampicillin resistance. The clone released a fragment of ~2150 bp when cut with EcoRI and BamHI and the presence of the mutations corresponding to the E148A and E150 mutations were confirmed with sequencing using primer oJH04.

pTG004 was generated with overlap extension PCR. The "UP" product was amplified from *B. subtilis 168* genomic DNA with primer pair oAS334/oAS335. The "DOWN" product was amplified from BTG68 with primer pair oAS336/ oAS337. The two PCR products were used as template for overlap extension PCR with primer pair oAS334/oAS337. The amplified fragment was cut with EcoRI and BamHI and cloned into pMiniMAD2 cut with the same enzymes.

pTG006 was generated with overlap extension PCR. The "UP" product was amplified from *B. subtilis 168* genomic DNA with primer pair oAS334/oAS335. The "DOWN" product was amplified from BTG87 with primer pair oAS336/oAS337. The two PCR products were used as template for overlap extension PCR with primer pair oAS334/oAS337. The amplified fragment was cut with EcoRI and BamHI and cloned into pMiniMAD2 cut with the same enzymes.

13

pYD216 was generated by cloning PCR product from oYD298 and oYD299 amplification of *B. subtilis 168* genomic DNA into pCH364 (EcoRI/BamHI).

pYD218 was generated by cloning PCR product from oYD298 and oYD299 amplification of *B. subtilis 168* genomic DNA into pKNT25 (EcoRI/BamHI).

pYD221 was generated by cloning PCR product from oYD479 and oYD480 amplification of *B. subtilis 168* genomic DNA into pKNT25 (EcoRI/BamHI).

pYD227 was generated by cloning PCR product from oYD475 and oYD480 amplification of *B. subtilis 168* genomic DNA into pKNT25 (EcoRI/BamHI).

pYD228 was generated with overlap extension PCR. The "UP" product was amplified from *B. subtilis 168* genomic DNA with primer pair oYD407/oYD546. The "DOWN" product was amplified from pJW006 with primer pair oYD409/ oYD545. The two PCR products were used as template for overlap extension PCR with primer pair oYD407/oYD409. The amplified fragment was cut with NheI and XhoI and cloned into pET24b cut with the same enzymes.

pYD229 was generated with overlap extension PCR. The "UP" product was amplified from *B. subtilis 168* genomic DNA with primer pair oYD298/oYD578. The "DOWN" product was amplified from pJW006 with primer pair oYD299/ oYD577. The two PCR products were used as template for overlap extension PCR with primer pair oYD298/oYD299. The amplified fragment was cut with EcoRI and BamHI and cloned into pKNT25 cut with the same enzymes.

pYD230 was generated with overlap extension PCR. The "UP" product was amplified from *B. subtilis 168* genomic DNA with primer pair oYD298/oYD578. The "DOWN" product was amplified from pJW006 with primer pair oYD299/ oYD577. The two PCR products were used as template for overlap extension PCR with primer pair oYD298/oYD299. The amplified fragment was cut with EcoRI and BamHI and cloned into pCH364 cut with the same enzymes.

REFERENCES

1. Duan Y, Sperber AM, Herman JK. 2016. YodL and YisK possess shape-modifying activities that are suppressed by mutations in *Bacillus subtilis mreB* and *mbl*. J Bacteriol 198:2074-88.
2. Dobihal GS, Brunet YR, Flores-Kim J, Rudner DZ. 2019. Homeostatic control of cell wall hydrolysis by the WalRK two-component signaling pathway in Bacillus subtilis. Elife 8.
3. Guo T, Herman JK. 2023. Magnesium modulates *Bacillus subtilis* cell division frequency. J Bacteriol 205:e0037522.
4. Koo BM, Kritikos G, Farelli JD, Todor H, Tong K, Kimsey H, Wapinski I, Galardini M, Cabal A, Peters JM, Hachmann AB, Rudner DZ, Allen KN, Typas A, Gross CA. 2017. Construction and Analysis of Two Genome-Scale Deletion Libraries for *Bacillus subtilis*. Cell Syst 4:291-305 e7.
5. Olson MG, Goldammer M, Gauliard E, Ladant D, Ouellette SP. 2018. A Bacterial Adenylate Cyclase-Based Two-Hybrid System Compatible with Gateway((R)) Cloning. Methods Mol Biol 1794:75-96.
6. Patrick JE, Kearns DB. 2008. MinJ (YvjD) is a topological determinant of cell division in *Bacillus subtilis*. Mol Microbiol 70:1166-79.
7. Szurmant H, Nelson K, Kim EJ, Perego M, Hoch JA. 2005. YycH regulates the activity of the essential YycFG two-component system in *Bacillus subtilis*. J Bacteriol 187:5419-26.

8. Szurmant H, Mohan MA, Imus PM, Hoch JA. 2007. YycH and YycI interact to regulate the essential YycFG two-component system in *Bacillus subtilis*. J Bacteriol 189:3280-9.
9. Sperber AM, Herman JK. 2017. Metabolism Shapes the Cell. J Bacteriol 199.